
Equilibrium and non-Equilibrium regimes in the learning of Restricted Boltzmann Machines

Aurélien Decelle^{1,2,†}

Cyril Furtlehner²

Beatriz Seoane^{1,*}

¹Departamento de Física Teórica, Universidad Complutense, 28040 Madrid, Spain.

²Université Paris-Saclay, CNRS, INRIA Tau team, LISN, 91190, Gif-sur-Yvette, France.

[†]adecelle@ucm.es; ^{*}bseoane@ucm.es

Abstract

Training Restricted Boltzmann Machines (RBMs) has been challenging for a long time due to the difficulty of computing precisely the log-likelihood gradient. Over the past decades, many works have proposed more or less successful training recipes but without studying the crucial quantity of the problem: the mixing time, i.e. the number of Monte Carlo iterations needed to sample new configurations from a model. In this work, we show that this mixing time plays a crucial role in the dynamics and stability of the trained model, and that RBMs operate in two well-defined regimes, namely equilibrium and out-of-equilibrium, depending on the interplay between this mixing time of the model and the number of steps, k , used to approximate the gradient. We further show empirically that this mixing time increases with the learning, which often implies a transition from one regime to another as soon as k becomes smaller than this time. In particular, we show that using the popular k (persistent) contrastive divergence approaches, with k small, the dynamics of the learned model are extremely slow and often dominated by strong out-of-equilibrium effects. On the contrary, RBMs trained in equilibrium display faster dynamics, and a smooth convergence to dataset-like configurations during the sampling. Finally we discuss how to exploit in practice both regimes depending on the task one aims to fulfill: (i) short k can be used to generate convincing samples in short learning times, (ii) large k (or increasingly large) is needed to learn the correct equilibrium distribution of the RBM. Finally, the existence of these two operational regimes seems to be a general property of energy based models trained via likelihood maximization.

1 Introduction

Restricted Boltzmann Machines (RBM) are one of the generative stochastic neural networks that have been available for decades [1] and are renowned for their capacity to learn complex datasets [2] and draw similar new data. Furthermore, the hidden correlations found in the data are easily accessible [3, 4, 5], which is particularly interesting for a scientific use of Big Data. Despite these positive features, RBMs still remain hard to train and evaluate, and hence to use in practical problems. In comparison, Generative Adversarial Network (GAN) [6] (for which it is much harder to find a working architecture) are more commonly used, not only because of the advantages given by convolutional layers, but also because the generative process does not depend on a costly sampling procedure with an uncontrolled convergence time.

Both training and data generation of RBMs are tricky and unpredictable in inexperienced hands. One of the main difficulties is that it is hard to evaluate if the learning is progressing or not. Yet, many works in the past twenty years have proposed recipes for good practices in RBM training [7]. Unfortunately, the evaluation of these recipes relies only on the comparison of the values reached by the log-likelihood (LL) [8, 7, 9], a quantity that cannot be monitored in tractable times during the learning process. Studies properly characterizing the quality, independence, or stability of the generated samples using the different recipes are nearly absent in the Literature. In fact, many works just show a set of new samples (for eye evaluation) that were either obtained after a short Markov Chain Monte Carlo (MCMC) sampling initialized at the dataset, or borrowed from the permanent chain (negative particle) at the end of the training [10]. In other studies, a reconstruction error after one or several MCMC steps is used to determine if the machine was correctly trained [11]. However, none of these measures guarantees that the trained model can generate from scratch new samples nor that the dataset are typical samples of that model. At most these tests assure you that samples of the dataset are locally stable w.r.t few MCMC steps, unless a proper decorrelation from the initial conditions or a link to equilibrium properties are investigated. Finally, more recent works use a classification score on the activation of the latent variables [12, 13], which reflects that the relevant features were learned, but is silent about the generative power of the machine.

RBMs are receiving an increasing attention in life and pure sciences during the recent years [5, 14, 15, 16, 17, 18, 19, 20, 21] given their potential for interpretability of the patterns learned by the machine (a rare feature in machine learning). Indeed, the RBM formalism enables the extraction of the (unknown) probability distribution function of the dataset. Yet, such an approach is meaningful if the dataset is related to the equilibrium properties of the trained model. Given these new and exciting perspectives for the RBMs, it is more than ever important to establish reproducible protocols and evaluation tools to guarantee not only that the model generates good enough data, but also that the dataset are typical equilibrium samples of the model.

In this work we demonstrate that the classical training procedures can lead to two distinct regimes of the RBM: an equilibrium and an out-of-equilibrium (OOE) one. A finding that had been recently discussed in the Literature under the name of convergent or non-convergent regimes in a different family of generative energy based models (EBMs), those whose energy function is a ConvNet [22]. Here, at variance to previous approaches, we show that the equilibrium regime is observed if the number of MCMC steps, k , used to estimate the LL gradient, is larger than the algorithm mixing time (MT). The latter emerges when k falls below this MT. In particular, we show that for a classical dataset such as MNIST, the MT is always rather large and grows with the learning time. This implies that learning an “equilibrium” model (i.e. a RBM that operates in the equilibrium regime) is costly, and that most of the works in the Literature operate without any doubt in the OOE regime. In this regime, the equilibrium distribution of the machine at the end of the learning is significantly different from that of the dataset. Yet, despite this handicap, we show the OOE regime can be exploited to generate good samples at short training times, an observation that have already been exploited in practice [23] for convolution EBM. All our conclusions rely on the study of 9 datasets: MNIST [24], whose results are discussed in the main-text, FashionMNIST [25], Caltech101 Silhouettes, small-NORB dataset [26], a human genome dataset [27] (with similar dimensions as MNIST but more structured), the high-quality CelebA [28] projected in black and white, and in low definition but in color, and CIFAR [29]. The analysis of most of the last datasets are discussed only in the SM and show a similar behavior to the one observed on MNIST.

Our paper is organized as follows. RBMs, their general principles and learning equations are defined in sec. 2. We review previous related works in sec. 3. In sec. 4 we define the different observables used to monitor the training and sampling. Finally, we discuss experimental results in sec. 5.

2 Definition of the model

An RBM is a Markov random field with pairwise interactions defined on a bipartite graph of two non-interacting layers of variables: the visible nodes, $\mathbf{v} = v_i, i = 1, \dots, N_v$, represent the data, while the hidden ones, $\mathbf{h} = h_j, j = 1, \dots, N_h$, are the latent representations of this data and are there to build arbitrary dependencies between the visible units (see sketch in fig. 1–A). Usually, the nodes are binary-valued in $\{0, 1\}$, yet Gaussian or more arbitrary distributions on real-valued bounded support are also used, ultimately making RBMs adaptable for more heterogeneous datasets. Here, we deal only with binary $\{0, 1\}$ variables for both the visible and hidden nodes. Other approaches

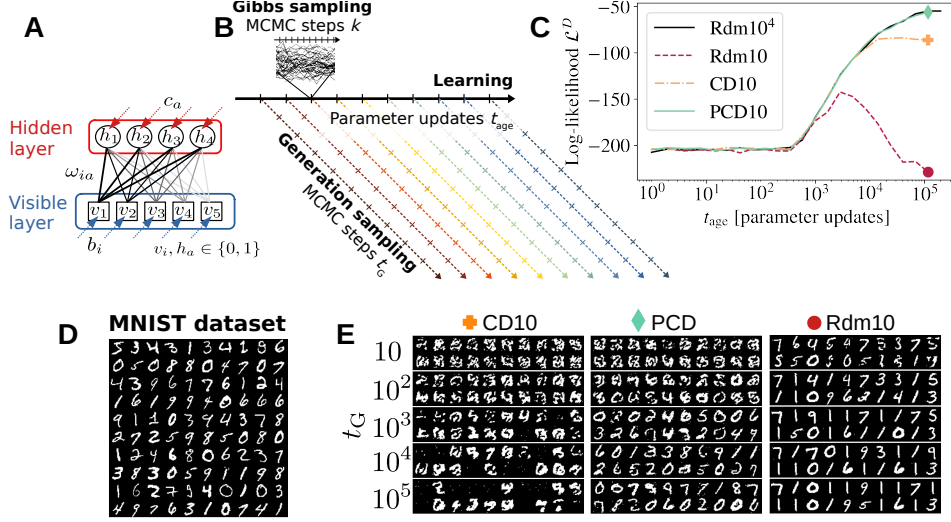


Figure 1: Sketch of an RBM in **A** and of the pipeline of our analysis in **B**. **C** Evolution of the LL of the dataset during the learning for 4 different RBMs trained using either a very long MCMC sampling to estimate the gradient ($k = 10^4$, Rdm- 10^4) or short samplings $k = 10$ following different recipes for the initialization of the MC chains (CD-10, PCD-10 and Rdm-10). The large symbols mark the LL of the RBMs used to generate new samples in **E**. In **D** we show a subset of the MNIST database, and in **E** a subset of the samples drawn by the $k = 10$ RBMs marked in **C** through a MCMC sampling of the equilibrium Gibbs measure initialized at random and after $10, 10^2, 10^3, 10^4$ and 10^5 MCMC steps. Note that in our setup the MC chain are initialized at random, and we can observe that RBMs trained with CD-10 do not converge to any digit despite reaching higher value of the LL than Rdm10 which instead manage to create digits quite fast. Also note the lack of diversity of Rdm10 for large sampling time.

using truncated-Gaussian hidden units [30], giving a ReLU type of activation functions for the hidden layer do work well, but in our experiments we observed qualitatively the similar dynamical behavior and therefore we will stick to binary hidden units for the rest of the article. The energy function of an RBM is taken as

$$E[\mathbf{v}, \mathbf{h}; \mathbf{w}, \mathbf{b}, \mathbf{c}] = - \sum_{ia} v_i w_{ia} h_a - \sum_i b_i v_i - \sum_a c_a h_a, \quad (1)$$

with \mathbf{w} the weight matrix and \mathbf{b}, \mathbf{c} the visible and hidden biases, respectively. The Boltzmann distribution is then given by

$$p[\mathbf{v}, \mathbf{h} | \mathbf{w}, \mathbf{b}, \mathbf{c}] = \frac{\exp(-E[\mathbf{v}, \mathbf{h}; \mathbf{w}, \mathbf{b}, \mathbf{c}])}{Z} \quad \text{with } Z = \sum_{\{\mathbf{v}, \mathbf{h}\}} e^{-E[\mathbf{v}, \mathbf{h}]}, \quad (2)$$

being the partition function of the system. RBMs are usually trained using gradient ascent of the LL function of the training dataset $\mathcal{D} = \{\mathbf{v}^{(1)}, \dots, \mathbf{v}^{(M)}\}$, being the LL defined as

$$\mathcal{L}(\mathbf{w}, \mathbf{b}, \mathbf{c} | \mathcal{D}) = M^{-1} \sum_{m=1}^M \ln p(\mathbf{v} = \mathbf{v}^{(m)} | \mathbf{w}, \mathbf{b}, \mathbf{c}) = M^{-1} \sum_{m=1}^M \ln \sum_{\{\mathbf{h}\}} e^{-E[\mathbf{v}^{(m)}, \mathbf{h}; \mathbf{w}, \mathbf{b}, \mathbf{c}]} - \ln Z. \quad (3)$$

The gradient is then composed of two terms: the first accounting for the interaction between the RBM's response and the training set, and same for the second, but using the samples drawn by the machine itself. The expression of the LL gradient w.r.t. all the parameters is given by

$$\frac{\partial \mathcal{L}}{\partial w_{ia}} = \langle v_i h_a \rangle_{\mathcal{D}} - \langle v_i h_a \rangle_{\mathcal{H}}, \quad \frac{\partial \mathcal{L}}{\partial b_i} = \langle v_i \rangle_{\mathcal{D}} - \langle v_i \rangle_{\mathcal{H}} \quad \text{and} \quad \frac{\partial \mathcal{L}}{\partial c_a} = \langle h_a \rangle_{\mathcal{D}} - \langle h_a \rangle_{\mathcal{H}}, \quad (4)$$

where $\langle f(\mathbf{v}, \mathbf{h}) \rangle_{\mathcal{D}} = M^{-1} \sum_m \sum_{\{\mathbf{h}\}} f(\mathbf{v}^{(m)}, \mathbf{h}) p(\mathbf{h} | \mathbf{v}^{(m)})$ denotes an average over the dataset, and $\langle f(\mathbf{v}, \mathbf{h}) \rangle_{\mathcal{H}}$, the average over the Boltzmann measure in Eq. 2.

A large part of the literature on RBMs focuses on schemes to approximate the r.h.s. of Eqs. 4. In theory, these terms can be computed up to an arbitrary precision using parallel MCMC simulations as long as the number of MC steps are large enough to ensure a proper sampling of the equilibrium configuration space. In other words, sampling times should be larger than the MCMC MT. A naive way to implement this idea is to initialize each of these parallel Markov chains on random conditions, perform k MCMC steps, and use the final configurations to estimate the gradient. We call this scheme **Rdm-k**. This scheme is not used in practice because it would require too many k steps if the MT is too large. Many recipes have been proposed to shorten this sampling and approximate the negative term of the gradient, but since the introduction of the so-called contrastive divergence (CD) by Hinton [31], only a limited number of schemes are used in practice. The first one, **CD-k**, initializes the MCMC simulation from the same data of the mini-batch used to compute the gradient, and performs $k \sim \mathcal{O}(1)$ sampling steps. This approximation relies on the idea that the dataset must be a good approximation of the equilibrium samples of a well trained RBM, something that is not true for a poorly trained machine, whose typical samples are quite distant from the dataset. In the second commonly used method, the last configurations of the Markov chains are saved from one parameter update to the other, and then used to initialize the subsequent chain. As in the other methods, k MCMC steps are used to estimate the gradient for each update. This method is known as persistent-CD: **PCD-k** [32], and takes advantage of the fact that the RBM’s parameters change smoothly during the learning and the same is expected for the models’ equilibrium distribution¹. Finally, other approximations, such as mean-field or TAP equations [10], or more elaborate approaches, such as the parallel tempering technique [33, 34], can be used. A common feature of all these recipes is that they rely on very few simulation steps to sample the Boltzmann distribution, and the trained model often generates rather bad configurations.

To illustrate this last comment, let us discuss a provocative experiment shown on fig. 1–E where we try to sample new digits just by sampling the equilibrium measure of our trained RBMs using a MCMC initialized uniformly at random. Let us stress that this is not the standard set-up used in the field to generate new samples, but it is a strong test of the generation power of the trained model. We compare the outcome of the generated samples (as function of the sampling time) for three RBMs trained each following different recipes to compute the negative term of the gradient: CD-10, PCD-10 and Rdm-10. At this point, $k = 10$ might seem a very small number. It is however the typical order of magnitude used in the Literature. The details of the learning protocol are discussed later in the text and summarized in the SM. The first striking point on fig. 1–E, is the inability of the CD-10 RBM to properly sample digits in this set-up. This problem has been reported before [35, 8], but since CD is part of the standard methods, we want to insist on this point. In addition, PCD-10 trained RBM generates proper digits but only after a very long sampling time, while with Rdm-10, quite surprisingly, digits are properly generated after only 10 MCMC steps. Yet, samples obtained after much longer MCMC steps have unbalanced digits representations, like the 1 being over-represented. In fact, we observe that poorly trained models generate samples that do not respect the correct balance between the 10 digits present in the original database (see fig. 1–D). We already mentioned the 1s in the Rdm-10 run, but it happens the same (to a lesser extent) with the 0 in the PCD-10 case. Alternatively to these generated samples, we show the evolution of the LL during the learning of these same three RBMs in fig. 1–C. By definition of the loss function, the LL is intended to be maximized, so it constitutes a traditional measure of the quality of the training. The LL of the models used for the sampling of fig. 1–E are highlighted in large symbols. This plot illustrates the lack of reliability of the LL to monitor the quality of the learning. For instance, CD-10 reaches quite high values of LL and yet, it cannot generate a single digit. For the Rdm-10 is the other way around, it generates decent samples but with a very poor LL. Finally, we observe that the LL of PCD-10 reaches very high values, comparable to RBMs trained using up to $k = 10^4$ MCMC steps to estimate the gradient. We will come back to this point. Our experiment highlights, first, that the LL cannot be used all alone to quantify the generative power of an RBM, and second, that the quality of the generated samples may variate in a non-monotonic way during the generation sampling.

¹This adiabatic scheme is thus valid as long as the relaxation time for the RBM parameters during the learning is much larger than the MCMC mixing times.

3 Related works

Recent years have witnessed a large number of studies trying to understand and control the learning of RBMs. In these works, meta-parameters are varied at the same time that an approximation of the LL [8, 36] of the train/test set is monitored throughout the learning process. The stability of the evolution of the LL and the maximum value achieved, are then used to compare the different recipes and parameters. For instance, in Ref. [8] the LL of different learning schemes are evaluated and the samples inspected visually. Unfortunately, no estimator is used to assess the quality of the samples, neither is clear the precise protocol used to generate these samples. In Ref. [9], the authors investigate the stability of the learning of RBMs with binary inputs² by comparing the learned features. They show (using mostly the LL and an eye inspection of the learned features) that a centered version of the gradient can be much stabler. In Ref. [7], the authors study, in a systematic way, the convergence properties of CD, PCD and PT on several small toy models that can be analyzed exactly, that is, where the LL can be computed by brute-force. We can find more recent works [37, 38, 39, 40] improving the learning scheme for RBMs and yet, still not giving much information about the quality of the generated samples nor the equilibrium properties of the trained models. In our results below, we will show that without putting on the table this information, the comparison between methods or tuning of parameters, becomes extremely unstable. Finally, we want to mention that it is particularly surprising that the CD recipe (with short k) is still used [41, 42, 43, 39]. As shown, RBMs trained with CD are not able to generate proper samples from scratch. And this behavior is true even if doing $k \approx O(100)$ MC steps at each update. The classical explanation for this is that CD is creating local energy well around the datapoint which are separated by large energy barriers [35], since the dynamics do not have time to relax when k is small.

In the rest of the paper, we explain how, by characterizing the MT, we are able to explain the capricious behavior of RBMs with respect to the different usual schemes. Furthermore, we will see that our results are totally consistent to what is observed in other families of EBM such as ConvNet generative networks [23, 22] or Boltzmann Machines [44, 45] when trained using short k negative chains, which suggests that this explanation applies to EBMs in general.

4 Monitoring the learning performance of RBMs

In this work we wish to address the following questions: (i) How can one quantify that an RBM has correctly learned a dataset? (ii) has it learned the equilibrium model? (iii) when should one stop the learning and the sampling of new configurations? We already argued in sec. 2 that, alone, the LL of the dataset is not precise enough to address these questions. For this reason, we have considered several additional observables to quantify the generated samples' quality. We introduce shortly below the different metrics used in our analysis, the precise definitions of all of them can be found in the SM. All the observables are computed and averaged using sets of $N_s = 1000$ true or generated samples.

Log-likelihood \mathcal{L} : On the contrary to other machine learning methods (such as classification), the LL cannot be exactly evaluated in an RBM without an exhaustive search of the configuration space. Thus we estimate the partition function using the Annealed Importance Sampling (AIS) method [46]. Details of our implementation can be found in SM. We call \mathcal{L}^D the LL of the (original) dataset with respect to the model, and \mathcal{L}^{RBM} , the LL of the generated samples with respect to the model.

Error of the second moment $\mathcal{E}^{(2)}$: we compute the mean square error (MSE) between the covariance matrix computed with a set of samples generated by the RBM and one of the dataset.

Error in the power spectral density \mathcal{E}^{PSD} : For images, we compute the log average power spectrum function of radial wave number distance for both a subset of the dataset and the generated set, and then compute the MSE between the two functions. In practice, we compute the error (between true and generated samples) on the logarithm of the squared module of the image's discrete 2D-Fourier transform elements A_{kl} at a fixed distance d in Fourier space

$$P(d) = \log \left(\langle \|A_{kl}\|^2 \rangle_{(k,l)|k^2+l^2=d^2} \right). \quad (5)$$

²It has been observed in MNIST that by flipping the input $0 \longleftrightarrow 1$, the usual gradient ascent was much slower in one case than in the other.

Error in the Adversarial Accuracy Indicator (AAI) \mathcal{E}^{AAI} : The AAI was recently introduced in Ref. [47] with the goal of quantifying the resemblance and the “privacy” of data drawn by a generative model with respect to the training set. This metric is based on the idea of data nearest neighbors. We begin by defining two sets containing, each one, N_s samples: (i) a “target” set containing only generated samples $T \equiv \{\mathbf{v}_{\text{RBM}}^{(m)}\}_{m=1}^{N_s}$ and (ii) a “source” with samples from the dataset $S \equiv \{\mathbf{v}_{\mathcal{D}}^{(m)}\}_{m=1}^{N_s}$. Then, for each sample m in groups $\{T, S\}$, we compute the closest sample—using the euclidean distance—to the set groups $\{T, S\}$. For instance, the closest samples in $\{S\}$ for a sample m in $\{T\}$ would be $d_{TS}(m) = \min_n \|\mathbf{v}_{\text{RBM}}^{(m)} - \mathbf{v}_{\mathcal{D}}^{(n)}\|$. We can compute in the same way $d_{ST}(m)$, $d_{SS}(m)$ and $d_{TT}(m)$. Once we have all these 4 distances, we can estimate how often the “nearest neighbor” (the sample at the shortest distance) of each sample is contained in the same starting set, or in the other one. When the generated samples are statistically indistinguishable from real ones, both frequencies should converge to the value of a random guess 0.5 when N_s large. We therefore compute the MSE of these two frequencies with respect to the asymptotic value 0.5, which defines \mathcal{E}^{AAI} . See SM for more details.

Relative entropy ΔS : We approximate the entropy of a given set of data by its byte size when compressed using gzip [48]. In particular, we compute the entropy of a group of N_s random samples of the dataset, $S^{\mathcal{D}}$, and the entropy of another set of data of the same size, called S^{cross} , composed in equal portions by samples of the train and generated set. Finally, we compute the relative size of this cross set with respect to the dataset’s one, minus the expected value for identical sets, i.e. $\Delta S = S^{\text{cross}}/S^{\mathcal{D}} - 1$. Then, a large ΔS indicates us that the generated set is less “ordered” than the dataset. On the contrary, a small ΔS reflects that the generated samples lack diversity.

In the SM, we show the evolution of other quality images observables along the generation sampling (such as the error in the third moment correlations, the error in the energy, or the Frechet Inception Distance score [49] for images). All them showing very similar trends to the ones shown here.

5 Results

Equipped with this set of quality measures, we now want to monitor and evaluate the learning process. To this end, we need to control precisely the learning dynamics and its interplay with the equilibration time. To do so, we try to isolate all the different factors affecting the learning, and for this reason, at a first stage, we avoid using the common tricks to speed up the estimation of the r.h.s. of the gradient of Eqs.4 during the learning. With this goal, we focus our first experiments on the Rdm-k schemes, and discuss the interplay with standard methods such as CD or PCD later on. The Rdm-k scheme is very practical to study the convergence to equilibrium for two reasons: (i) the MCMC chains are initialized from configurations that are uncorrelated with the dataset, and (ii) the sampling protocol used during the learning is identical to the one used to generate new samples from scratch with the learned RBM. The pipe-line of our experiments is summarized in Fig. 1–B. We split the analysis in two separated stages: learning and generation sampling. During the learning, we update the parameters for $\sim 2 \cdot 10^5$ times using the gradient estimated following the Rdm-k scheme (with $k = 10, 50, 100, 500, 10^3$ and 10^4). We save the RBM parameters at different numbers of updates equally spaced in logarithmic scale. The number of updates used to train a particular RBM will be referred as its *age*, t_{age} . During the generation stage, we sample the equilibrium Gibbs measure of each RBM (of age t_{age}) with a MCMC initialized at random. We evaluate the quality of the samples generated at Gibbs sampling times t_G equally spaced in logarithmic scale. Unless something else is mentioned, we will consider RBMs with $N_h = 500$ hidden nodes and trained with a fixed learning rate of $\eta = 0.01$, hence the different RBMs will differ only by the value of k and t_{age} . Further details on the learning parameters can be found in SM.

Evolution of the quality of the generated samples with the sampling time—

We show in Fig. 2–A the evolution of the quality estimators of the generated samples throughout the generation sampling for RBMs of different ages (i.e. following the different color lines in Fig. 1–B), and trained with three different k . We recall that perfect samples, in the sense that they are indistinguishable from the dataset, would have a score 0 in all the quality observables except for the LL, where \mathcal{L}^{RBM} should match $\mathcal{L}^{\mathcal{D}}$ ($\mathcal{L}^{\mathcal{D}}$ is marked as a horizontal line). For all k and early learning times (ages below $\lesssim 10^3$ updates in red-yellowish colors), all the metrics describe a constant behavior with t_G at roughly the same values obtained using a completely untrained RBM, and generally far away

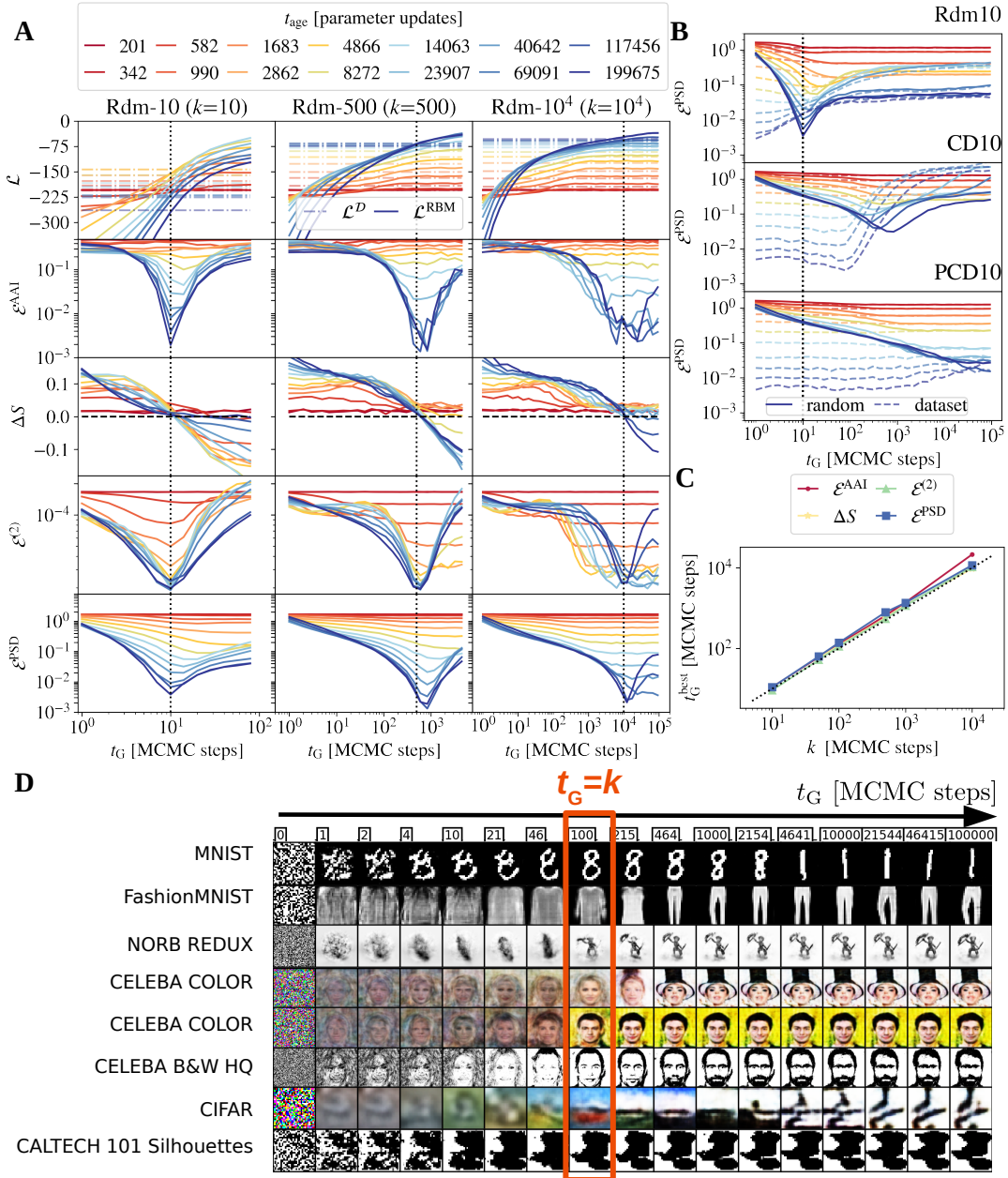


Figure 2: Evolution of the quality of the generated samples during the data generation sampling (along the color dashed lines of Fig. 1–B). In **A** we show the LL and the rest of quality estimators (introduced in Sect. 2) as function of the sampling time, t_G , for chains initialized at random and using RBMs trained for an increasing number of updates t_{age} (age is coded by colors) using the Rdm- k scheme with $k = 10, 500, 10^4$. In general, the closer \mathcal{E} and ΔS are to zero, the more similar the generated and original datasets are. For the LL, we show the value computed with the generated set (\mathcal{L}^{RBM} , in continuous growing lines) and with the original dataset (\mathcal{L}^D , in dashed horizontal lines). We observe that these two measures cross at roughly the same t_G at which all \mathcal{E} reach a minimum and ΔS crosses zero. **B** We show the evolution of ϵ^{PSD} for 3 RBMs trained using the Rdm-10, CD-10 and PCD-10 recipes, for the same ages as in **A**. We consider two possible initializations of the Markov chain (random in full lines and dataset in dashed lines). **C** We plot the position of the best performance peak and the time at which $\Delta S = 0$, as function of the number of MCMC steps k used for estimating the negative term of the gradient during the training. **D** We show an example of the images generated as function of t_G , using RBMs trained with Rdm-100 and with different datasets. The sampling time t_G that matches k is highlighted in an orange frame.

from 0. For an intermediate range of ages (pale blue colors), we observe an important improvement of the metrics with the RBM’s age, up to a certain value (dark blue lines) above which time evolution curves start to collapse. Furthermore, for $k = 10$, only young ages converge to constant curves in t_G , something that extends to intermediate ages for $k = 500$ and covers the majority of the ages for $k = 10^4$. In all the cases, the sampling of the oldest machine ($t_{\text{age}} \sim 200\text{k}$ updates) describe a non-monotonous behavior in the quality measures, with a clear peak of best quality at $t_G \sim k$. This is also the point where $\mathcal{L}^{\mathcal{D}}$ and \mathcal{L}^{RBM} intersect and where ΔS crosses 0. In Fig. 2–C, for each learning process using a different k , we plot the position of this t_G^{best} (obtained for each quality metrics) against the value of k used to train the machine. We observe a perfect match between both times. At this point we want to stress that we obtain exactly the same qualitative behavior with the other considered datasets, as shown in the SM. Fig. 2–C reflects that these RBMs “memorize” the number of MCMC steps used to estimate the gradient during the learning phase. Memory effects are a clear signal of non-equilibrium effects [50] and in fact, this effect is not present as long as k is long enough to equilibrate the system during the learning. Indeed, we see that the larger k , the longer (in terms of number of updates) it takes to observe memory effects (for $k = 10^4$ we only appreciate out-of-equilibrium effects above 100k updates, while they appear around $t_{\text{age}} \gtrsim 10^3$ updates in the case of $k = 10$). These two regimes (equilibrium and OOE) are also reproduced when using the CD and PCD schemes during the learning. We show in Fig. 2–B the evolution of \mathcal{E}^{PSD} of the generated samples as function of t_G for 3 RBMs trained with the 3 schemes and $k = 10$ steps (higher values of k are shown in the SM). We compare results with MCMC chains initialized either at random (continuous lines) or at the dataset (dashed lines). The sampling of the RBMs trained with CD-10 is also highly complex in time, and much slower than that of the Rdm-10 considering that the values of \mathcal{E}^{PSD} measured in runs from random initialization and from the dataset never converge to the same values for large t_{age} . The situation is rather different for PCD-10, where the error sampling curves describe a very smooth behavior in time and a very slow convergence towards an equilibrium value. Yet According to the minimum values reached in \mathcal{E}^{PSD} , the equilibrium samples of that model are significantly worse than the best samples created using the Rdm scheme (even working in the OOE regime). This difference is observed also in the rest of quality estimators and at much higher values of k , as shown in Fig. 5 of the SM. Indeed, for MNIST, one needs to reach PCD- 10^3 to start to match the qualities achieved with the Rdm-10 recipe when exploiting the OOE regime.

Quantifying the mixing time: At this point, we try to quantify the MT or relaxation time of the MCMC dynamics of our RBM as a function of t_{age} , to rationalize figs. 2. To do so, we compute the time-autocorrelation function, ρ , of the averaged visible variables

$$\rho(t) = \frac{C_m(t)}{C_m(0)}, \text{ where } C_m(t) = \frac{1}{N_v} \sum_i (m_i(t) - \bar{m}_i)(m_i(0) - \bar{m}_i) \quad (6)$$

where $m_i(t) = \text{sigmoid}(\sum_a w_{ia} h_a(t) + b_i)$ and \bar{m}_i is the equilibrium magnetization.³ At this point, let us stress that in a perfectly trained RBM, \bar{m}_i would be equal to $1/N_v \sum_m v_i^{(m)}$. Yet, this is not the case in a poorly trained machine. For this reason, we estimate these equilibrium values from a long 10^5 MCMC steps simulation. The value of $\rho(t)$ will be close to 1 if the data at $t = 0$ and t are very similar, and to 0 if they are completely decorrelated. In order to measure properly the MT, we need to compute the autocorrelation function from equilibrium configurations. Therefore, we measure ρ with Eq. (6) but after discarding the first MCMC $\approx 10^4$ steps⁴. We show the time-correlation curves obtained for our best trained machine (using Rdm and $k = 10^4$) in Fig. 3–A for different values of t_{age} . Clearly, the older the machine, the slower the relaxation. Such a study is harder with the poorly trained RBMs because equilibration is achieved at times $t_G > 10^5$ for most of the t_{ages} , being particularly dramatic for Rdm-10 where relaxations are extremely slow, see SM. The decay being typically exponential, we can easily extract the MT (or the exponential relaxation time), t_α , from a fit of $\rho(t)$ to $A \exp(-t/t_\alpha)$. We show the dependence of t_α with t_{age} in Fig. 3–C. This t_α (for the slowest observable) controls the time-scale of the relaxations in the system, the time necessary to sample independent (uncorrelated) configurations, which means that the number of MCMC iterations necessary to reach equilibrium from the beginning of a MCMC simulation is expected to scale with it. Typically, the thermalization time, t_{therm} , is some few times this t_α [51]. This means that, in order to guarantee a sampling of equilibrium configurations,

³The time-autocorrelation function of the visible, hidden or averaged hidden units are qualitatively the same.

⁴In practice, we discard as many MCMC steps as needed to stop detecting dependence on the $t = 0$ point.

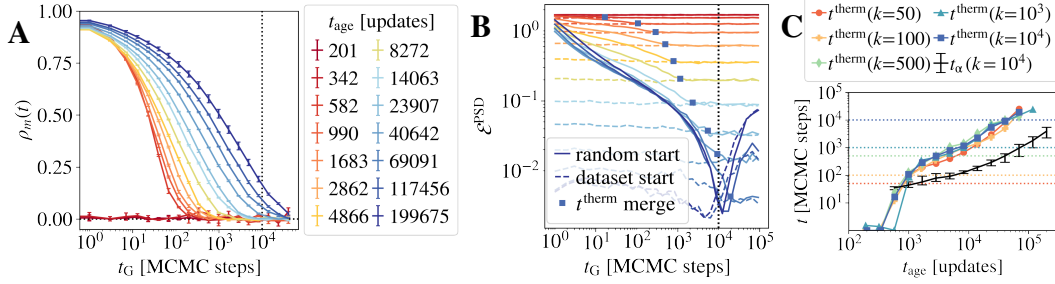


Figure 3: **A** The time-autocorrelation function of the visible mean magnetizations, ρ_m (see Eq. (6)), computed during the sampling of an RBM trained with Rdm- 10^4 for different number of updates t_{age} . This function carries the information about the number of MCMC steps that are needed (in equilibrium) to forget a initial configuration of the MC chain. Clearly, the time needed to decorrelate grows with the age of the RBM. In **B**, for the same RBMs, we show the evolution of the generated samples' quality through the \mathcal{E}^{PSD} observable, as function of the sampling time t_G , and for two different initializations: from the dataset and from random. We mark the times t^{therm} beyond which both runs converge to the same constant value. **C** We compare the mixing times, t_α , obtained from a fit of the curves $\rho_m(t)$ in **A** to the form $\exp(-t/t_\alpha)$, with the convergence-to-equilibrium times t^{therm} obtained in **B** for RBMs trained with different values of k . We see that the equilibration time t^{therm} follow the same trend for various values of k .

one needs Gibbs samplings longer than this t_{therm} (which scales with t_α). Note that t_{therm} (the distance to equilibrium) might depend on the MC starting point while t_α should not, yet t_{therm} will grow proportionally with t_α for any learning scheme. In fact, we can estimate independently the thermalisation time for the Rdm- k runs, t_{therm} , by comparing results from two independent simulations with different initializations: random and dataset, and wait until they converge to the same equilibrium expectation value. This means that one can estimate t_{therm} (for each t_{age}) by the number of MCMC steps needed to collapse the measures of the two trajectories to a constant value. See for instance Fig. 3–B, where we show the evolution of \mathcal{E}^{PSD} with t_G for the two runs. The merging point for each t_{age} is highlighted with a square. We show the t_{therm} values we obtain with this procedure in Fig. 3–C for the different values of k .

As a result, these two times, t_α and t_{therm} , provide us with a lower and a safe upper bound (for instance, when initializing at random) for the minimum number of MCMC steps (for the learning's Gibbs sampling), k , needed to learn a good equilibrium RBM model. As shown in Fig. 3–C, these times grow progressively with t_{age} , and in particular, falling always out of the range of iterations used to train the $k = 10$ runs (once the RBM starts to learn the dataset for $t_{\text{age}} \gtrsim 10^3$ updates), and falling out the range of scheme Rdm-500 for $t_{\text{age}} \gtrsim 10^4$ and for the last 2 t_{age} for the Rdm- 10^4 scheme (i.e. for $t_{\text{age}} \gtrsim 10^5$ updates). In other words, at those ages, the learning enters in the OOE regime and the RBM starts to learn the dynamical process rather than the equilibrium properties. In fact, these ages mark the crossover between smooth and non-monotonic evolution of the observables in Fig. 2–A. This reinforces our previous claim that the apparition of the “best performance peak” in the error estimators is a purely non-equilibrium effect. A similar comment can be made for the LL. See for instance Fig. 2–A first row, for each t_{age} , we compare the LL measured on the generated \mathcal{L}^{RBM} and original dataset \mathcal{L}^{D} as function of its generation sampling time t_G . We distinguish, again, two distinct behaviours associated to the equilibrium or OOE regime. In the first case, the LL of the generated samples converges to the value of the dataset and remain there even at large t_G . Whereas, in the OOE regime, \mathcal{L}^{RBM} crosses \mathcal{L}^{D} at $t_G \approx k$ and continues growing afterwards. This highlights the problem of using the LL to evaluate the sample generation power. While the fact that the likelihood increases during the learning is in general a good sign, it is not necessarily linked with the equilibrium properties of the model. In fact, the observation that \mathcal{L}^{RBM} tends to reach much higher values than \mathcal{L}^{D} should be rather interpreted as a sign of poor learning, as shown in Fig. 1.

As a direct consequence of the results discussed above, we can see that even in the case where sampling is openly OOE, such as with the Rdm-10 scheme, one can generate fairly good samples as long as one limits the generation sampling to $t_G \sim k$, as shown in Fig. 1 for $k = 10$: digits are reproduced with uniform probability, and they look OK on visual inspection. For longer samplings

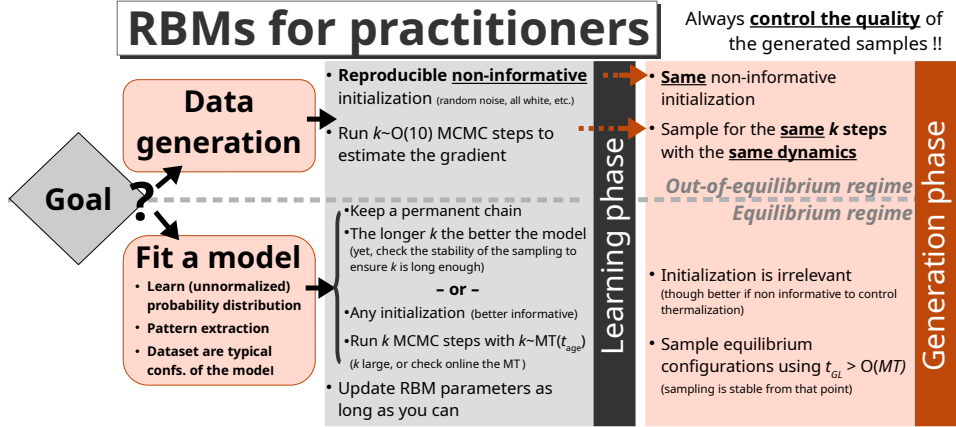


Figure 4: Flow chart of the algorithm proposed to train and sample properly an RBM depending on the final goal of the training.

we start to get clear unbalanced distributions. It is also quite remarkable that when matching t_G with k in the OOE regime of Rdm schemes, we get better quality samples than with the standard CD or PCD schemes even at very long sampling times, as we can see from the comparison of \mathcal{E}^{PSD} in Fig. 2–B. This is also true for other quality observables or larger values of k as shown around Fig. 5 of the SM. In particular, for MNIST, the OOE recipe always generates better samples than the equilibrium regime reached with PCD trained with $k < 10^3$ steps.

6 Conclusions

In this work, we show that the training of an RBM is richer and more complex than what previously thought. We show that the choice of the number of MCMC steps, k , used to estimate the gradient during the learning has a dramatic impact on the learned model’s dynamics and equilibrium states. In practice, we find two regimes: (i) the OOE, when k is much lower than the MCMC mixing time, the trained RBM model encodes the dynamical process followed to train it, resulting in a highly non-linear, unstable and slow evolution of the quality of the generated samples with the sampling time, and a convergence towards poor and strongly biased samples. And (ii) the equilibrium regime, when k overpasses largely the mixing time, the marginal equilibrium probability distribution of the trained model (over the visible layer) matches that of the dataset. In such case, the quality of the generated samples improves smoothly in time converging faster to the equilibrium values, converging much faster than in the OOE regime. While regime (ii) is needed to obtain good trained models, we show that regime (i) is particularly well suited for sample generation because the data sampling non-linearities can be controlled in the Rdm- k approach, and exploited to generate high-quality data in short training times. We further show that the MC mixing time increases significantly as the learning progresses, being always much larger than the standard k s used in the Literature. We summarize the best strategy to train and exploit RBMs depending on their purpose in Fig. 4.

The existence of a crucial competing mechanism in the training process had already been noted and exploited in EBMs with more complex energy functions (those defined with deep convolutional neural networks) [22, 23], and after our results, both regimes were also found in the simpler brother of the RBMs, the Boltzmann Machines [44, 45]. This evidences that the OOE regime, which was widely unnoticed in the Literature for decades, is a general consequence of the MCMC based likelihood maximization methods, so it is expected to be reproduced in many other popular models like Deep Boltzmann Machine (DBM). Interestingly, our results should simplify their training and use, at least in the OOE regime. More generally, this work provides a set of key points to be checked when working with EBMs, and a new fundamentally distinctive attribute to these generative models: equilibrium or OOE. We leave for future works systematic comparisons between the models trained in each of these regimes, and in particular, the effect on the features. For instance, we observed that RBMs trained with low k suffer strong aging effects extremely similar to those observed on the spin glasses [52]. Effects which are not present in equilibrium RBMs.

Acknowledgments and Disclosure of Funding

A.D. and B.S. were supported by the Comunidad de Madrid and the Complutense University of Madrid (Spain) through the Atracción de Talento program (Refs. 2019-T1/TIC-13298 and Ref. 2019-T1/TIC-12776). BS was also partially supported by MINECO (Spain) through Grant No. PGC2018-094684-B-C21 (partially funded by FEDER).

References

- [1] Paul Smolensky. Information processing in dynamical systems: Foundations of harmony theory. Technical report, Colorado Univ at Boulder Dept of Computer Science, 1986.
- [2] Nicolas Le Roux and Yoshua Bengio. Representational power of restricted boltzmann machines and deep belief networks. *Neural computation*, 20(6):1631–1649, 2008.
- [3] R.D. Hjelm, V.D. Calhoun, R. Salakhutdinov, E.A. Allen, T. Adali, and S.M. Plis. Restricted Boltzmann machines for neuroimaging: an application in identifying intrinsic networks. *NeuroImage*, 96:245–260, 2014.
- [4] X. Hu, H. Huang, B. Peng, J. Han, N. Liu, J. Lv, L. Guo, C. Guo, and T. Liu. Latent source mining in fmri via restricted Boltzmann machine. *Human brain mapping*, 39(6):2368–2380, 2018.
- [5] Jérôme Tubiana, Simona Cocco, and Rémi Monasson. Learning protein constitutive motifs from sequence data. *Elife*, 8:e39397, 2019.
- [6] Ian Goodfellow, Jean Pouget-Abadie, Mehdi Mirza, Bing Xu, David Warde-Farley, Sherjil Ozair, Aaron Courville, and Yoshua Bengio. Generative adversarial nets. In *Advances in neural information processing systems*, pages 2672–2680, 2014.
- [7] Asja Fischer and Christian Igel. Training restricted boltzmann machines: An introduction. *Pattern Recognition*, 47(1):25–39, 2014. Number: 1.
- [8] Ruslan Salakhutdinov and Iain Murray. On the quantitative analysis of deep belief networks. In *Proceedings of the 25th international conference on Machine learning*, pages 872–879, 2008.
- [9] Jan Melchior, Asja Fischer, and Laurenz Wiskott. How to center deep boltzmann machines. *The Journal of Machine Learning Research*, 17(1):3387–3447, 2016.
- [10] Marylou Gabrié, Eric W Tramel, and Florent Krzakala. Training restricted Boltzmann machine via the Thouless-Anderson-Palmer free energy. In *Advances in neural information processing systems*, pages 640–648, 2015.
- [11] Peter de Boves Harrington. Feature expansion by a continuous restricted boltzmann machine for near-infrared spectrometric calibration. *Analytica chimica acta*, 1010:20–28, 2018.
- [12] Huihui Shen and Hongwei Li. A gradient approximation algorithm based weight momentum for restricted boltzmann machine. *Neurocomputing*, 361:40–49, 2019.
- [13] Ramasamy Savitha, ArulMurugan Ambikapathi, and Kanagasabai Rajaraman. Online rbm: Growing restricted boltzmann machine on the fly for unsupervised representation. *Applied Soft Computing*, 92:106278, 2020.
- [14] Guido Montúfar. Restricted boltzmann machines: Introduction and review. In *Information Geometry and Its Applications IV*, pages 75–115. Springer, 2016.
- [15] Jing Chen, Song Cheng, Haidong Xie, Lei Wang, and Tao Xiang. Equivalence of restricted boltzmann machines and tensor network states. *Physical Review B*, 97(8):085104, 2018.
- [16] Aurélien Decelle, Giancarlo Fissore, and Cyril Furtlehner. Thermodynamics of restricted Boltzmann machines and related learning dynamics. *Journal of Statistical Physics*, 172(6):1576–1608, 2018.
- [17] Kai Shimagaki and Martin Weigt. Selection of sequence motifs and generative hopfield-potts models for protein families. *Physical Review E*, 100(3):032128, 2019.
- [18] Roger G Melko, Giuseppe Carleo, Juan Carrasquilla, and J Ignacio Cirac. Restricted boltzmann machines in quantum physics. *Nature Physics*, 15(9):887–892, 2019.

- [19] Moshir Harsh, Jérôme Tubiana, Simona Cocco, and Remi Monasson. ‘place-cell’emergence and learning of invariant data with restricted Boltzmann machines: breaking and dynamical restoration of continuous symmetries in the weight space. *Journal of Physics A: Mathematical and Theoretical*, 53(17):174002, 2020.
- [20] Burak Yelmen, Aurélien Decelle, Linda Ongaro, Davide Marnetto, Corentin Tallec, Francesco Montinaro, Cyril Furtlehner, Luca Pagani, and Flora Jay. Creating artificial human genomes using generative neural networks. *PLoS genetics*, 17(2):e1009303, 2021.
- [21] Barbara Bravi, Jérôme Tubiana, Simona Cocco, Rémi Monasson, Thierry Mora, and Aleksandra M Walczak. Rbm-mhc: A semi-supervised machine-learning method for sample-specific prediction of antigen presentation by hla-i alleles. *Cell systems*, 12(2):195–202, 2021.
- [22] Erik Nijkamp, Mitch Hill, Tian Han, Song-Chun Zhu, and Ying Nian Wu. On the anatomy of mcmc-based maximum likelihood learning of energy-based models. In *Proceedings of the AAAI Conference on Artificial Intelligence*, volume 34, pages 5272–5280, 2020.
- [23] Erik Nijkamp, Mitch Hill, Song-Chun Zhu, and Ying Nian Wu. Learning non-convergent non-persistent short-run mcmc toward energy-based model. *Advances in Neural Information Processing Systems*, 32:5232–5242, 2019.
- [24] Yann LeCun, Léon Bottou, Yoshua Bengio, and Patrick Haffner. Gradient-based learning applied to document recognition. *Proceedings of the IEEE*, 86(11):2278–2324, 1998.
- [25] Han Xiao, Kashif Rasul, and Roland Vollgraf. Fashion-mnist: a novel image dataset for benchmarking machine learning algorithms. *CoRR*, abs/1708.07747, 2017.
- [26] Yann LeCun, Fu Jie Huang, and Leon Bottou. Learning methods for generic object recognition with invariance to pose and lighting. In *Proceedings of the 2004 IEEE Computer Society Conference on Computer Vision and Pattern Recognition, 2004. CVPR 2004.*, volume 2, pages II–104. IEEE, 2004.
- [27] Vincenza Colonna, Qasim Ayub, Yuan Chen, Luca Pagani, Pierre Luisi, Marc Pybus, Erik Garrison, Yali Xue, and Chris Tyler-Smith. Human genomic regions with exceptionally high levels of population differentiation identified from 911 whole-genome sequences. *Genome biology*, 15(6):1–14, 2014.
- [28] Tero Karras, Timo Aila, Samuli Laine, and Jaakko Lehtinen. Progressive growing of gans for improved quality, stability, and variation. *CoRR*, abs/1710.10196, 2017.
- [29] Alex Krizhevsky, Geoffrey Hinton, et al. *Learning multiple layers of features from tiny images*. Technical Report TR-2009, University of Toronto, Toronto., 2009.
- [30] V. Nair and G.E. Hinton. Rectified linear units improve restricted Boltzmann machines. In *Proceedings of the 27th international conference on machine learning (ICML-10)*, pages 807–814, 2010.
- [31] Geoffrey E Hinton. Training products of experts by minimizing contrastive divergence. *Neural computation*, 14(8):1771–1800, 2002.
- [32] Tijmen Tieleman. Training restricted Boltzmann machines using approximations to the likelihood gradient. In *Proceedings of the 25th international conference on Machine learning*, pages 1064–1071, 2008.
- [33] Koji Hukushima and Koji Nemoto. Exchange monte carlo method and application to spin glass simulations. *Journal of the Physical Society of Japan*, 65(6):1604–1608, 1996.
- [34] Russ R Salakhutdinov. Learning in markov random fields using tempered transitions. In Y. Bengio, D. Schuurmans, J. Lafferty, C. Williams, and A. Culotta, editors, *Advances in Neural Information Processing Systems*, volume 22. Curran Associates, Inc., 2009.
- [35] Guillaume Desjardins, Aaron Courville, Yoshua Bengio, Pascal Vincent, and Olivier Delalleau. Tempered markov chain monte carlo for training of restricted boltzmann machines. In *Proceedings of the thirteenth international conference on artificial intelligence and statistics*, pages 145–152. JMLR Workshop and Conference Proceedings, 2010.
- [36] Yuri Burda, Roger Grosse, and Ruslan Salakhutdinov. Accurate and conservative estimates of mrf log-likelihood using reverse annealing. In *Artificial Intelligence and Statistics*, pages 102–110. PMLR, 2015.

- [37] Roger Grosse and Ruslan Salakhudinov. Scaling up natural gradient by sparsely factorizing the inverse fisher matrix. In *International Conference on Machine Learning*, pages 2304–2313. PMLR, 2015.
- [38] Oswin Krause, Asja Fischer, and Christian Igel. Population-contrastive-divergence: Does consistency help with rbm training? *Pattern Recognition Letters*, 102:1–7, 2018.
- [39] Enrique Romero, Ferran Mazzanti, Jordi Delgado, and David Buchaca. Weighted contrastive divergence. *Neural Networks*, 114:147–156, 2019.
- [40] Vidyadhar Upadhyaya and PS Sastry. Efficient learning of restricted boltzmann machines using covariance estimates. In *Asian Conference on Machine Learning*, pages 836–851. PMLR, 2019.
- [41] Ken-Ichi Aoki and Tamao Kobayashi. Restricted boltzmann machines for the long range ising models. *Modern Physics Letters B*, 30(34):1650401, 2016.
- [42] Alan Morningstar and Roger G Melko. Deep learning the ising model near criticality. *arXiv preprint arXiv:1708.04622*, 2017.
- [43] David Yevick and Roger Melko. The accuracy of restricted boltzmann machine models of ising systems. *Computer Physics Communications*, 258:107518, 2021.
- [44] Pierre Barrat-Charlaix, Anna Paola Muntoni, Kai Shimagaki, Martin Weigt, and Francesco Zamponi. Sparse generative modeling via parameter reduction of boltzmann machines: application to protein-sequence families. *Physical Review E*, 104(2):024407, 2021.
- [45] Anna Paola Muntoni, Andrea Pagnani, Martin Weigt, and Francesco Zamponi. adabmdca: Adaptive boltzmann machine learning for biological sequences. *arXiv preprint arXiv:2109.04105*, 2021.
- [46] Oswin Krause, Asja Fischer, and Christian Igel. Algorithms for estimating the partition function of restricted boltzmann machines. *Artificial Intelligence*, 278:103195, 2020.
- [47] Andrew Yale, Saloni Dash, Ritik Dutta, Isabelle Guyon, Adrien Pavao, and Kristin P Bennett. Generation and evaluation of privacy preserving synthetic health data. *Neurocomputing*, 416:244–255, 2020.
- [48] Andrea Baronchelli, Emanuele Caglioti, and Vittorio Loreto. Measuring complexity with zip-pers. *European journal of physics*, 26(5):S69, 2005.
- [49] Martin Heusel, Hubert Ramsauer, Thomas Unterthiner, Bernhard Nessler, and Sepp Hochreiter. Gans trained by a two time-scale update rule converge to a local nash equilibrium. *Advances in neural information processing systems*, 30, 2017.
- [50] Nathan C Keim, Joseph D Paulsen, Zorana Zeravcic, Srikanth Sastry, and Sidney R Nagel. Memory formation in matter. *Reviews of Modern Physics*, 91(3):035002, 2019.
- [51] Alan Sokal. Monte carlo methods in statistical mechanics: foundations and new algorithms. In *Functional integration*, pages 131–192. Springer, 1997.
- [52] Marc Mézard, Giorgio Parisi, and Miguel Angel Virasoro. *Spin glass theory and beyond: An Introduction to the Replica Method and Its Applications*, volume 9. World Scientific Publishing Company, 1987.

Supplementary material

Aurélien Decelle^{1,2,†}Cyril Furtlehner²Beatriz Seoane^{1,*}¹Departamento de Física Teórica, Universidad Complutense, 28040 Madrid, Spain.²Université Paris-Saclay, CNRS, INRIA Tau team, LISN, 91190, Gif-sur-Yvette, France.

†adecelle@ucm.es; *bseoane@ucm.es

Contents

1	Quality Observables: detailed definitions	2
1.1	Log-likelihood (LL)	2
1.2	Energy	2
1.3	Error of the second moment	2
1.4	Error of the third moment	3
1.5	Power spectrum density	3
1.6	Adversarial Accuracy Indicator	3
1.7	Entropy	4
1.8	Frechet Inception Distance score	4
2	Details of the RBM used for the training of MNIST	4
2.1	RBM details	4
2.2	Computer load	4
3	Additional results for MNIST	5
3.1	Rdm-k scheme	5
3.2	Relaxations of equilibrium and OOE models	5
3.3	CD-k scheme	9
3.4	PCD-k scheme	9
3.5	Comparisons between different training schemes	11
4	Results for a Human Genome dataset	12
5	Results for CelebA	16
6	Results for FashionMNIST	17

7	Results for Caltech101 Silhouettes	17
8	Results for smallNORB dataset	20
9	Results for CIFAR10 dataset	21
10	Results for CelebA dataset	22

The code used for the experiments can be found at [Github](#).

1 Quality Observables: detailed definitions

We detail here the different observables used to quantify the quality of the generated samples.

1.1 Log-likelihood (LL)

The likelihood is the most difficult observable to compute. In practice, the Annealed Importance Sampling (AIS) method [1] is often used, since, as soon as $N_v \gtrsim 30$, an exact enumeration of all the RBM's states becomes impossible. Some recent works have dedicated large efforts to understand this object [2], from which we can extract a generic method to compute a reasonable estimate. First, let us recall that AIS is based on a simulated annealing process where a configuration is gradually brought from temperature $T = \infty$ to $T = 1$ using a set of bridging distributions. We therefore define a temperature schedule: $\{\beta_k \equiv 1/T_k\}$ such that $0 = \beta_0 < \beta_1 < \dots < \beta_K = 1$. For each temperature, we define the transition operator, $T_k(\mathbf{v}', \mathbf{v})$ to bring a configuration \mathbf{v} to \mathbf{v}' varying the temperature according to the temperature schedule. In our case it is done using MC sampling layer-wise. In our experiment, we use as bridging distributions the following

$$p_k(\mathbf{v}, \mathbf{h}) = \frac{1}{Z_k} \exp(-\beta_k E(\mathbf{v}, \mathbf{h})). \quad (1)$$

For the rest, we follow [2], using a set of N_I initial configurations, and N_β equally-spaced intermediate temperatures to compute the estimation of the partition function.

In our work, we used a set of $N_\beta \in [10^4, 10^5]$ temperatures uniformly distributed in this interval (depending on the system size). Then, results are averaged over $N_I \in [1000, 10000]$ realizations.

1.2 Energy

Given a trained model, we can compare the mean energy

$$E[\mathbf{s}, \boldsymbol{\tau}; \mathbf{w}, \mathbf{b}, \mathbf{c}] = - \sum_{ia} v_i w_{ia} h_a - \sum_i b_i v_i - \sum_a c_a h_a, \quad (2)$$

of the generated and original samples, namely, E_{RBM} and $E_{\mathcal{D}}$. In a perfect set-up, E_{RBM} should be larger to $E_{\mathcal{D}}$ at the beginning of the generation sampling (when initialising at random) and converge to $E_{\mathcal{D}}$ at long times after equilibration. In practice, one observes that E_{RBM} goes below $E_{\mathcal{D}}$ at long sampling times if the machine was trained out of equilibrium. In order to quantify the generated sample quality, we find useful to track the error in the energy, \mathcal{E}^E , as the mean squared error (MSE) between both measures.

1.3 Error of the second moment

Firstly, we compute the averaged covariance matrix of the data representation sites $C_{ij} = \overline{\text{Cov}(v_i, v_j)}$ (with $\overline{(\dots)}$ the average over N_s independent samples). This matrix can be computed either using the original dataset, in which case we call it $C_{ij}^{\mathcal{D}}$, or the generated dataset, then called C_{ij}^{RBM} . Once having both matrices, we estimate the distance between both kinds of C_{ij} at each

combination i, j through the MSE (which is equivalently the square of the Frobenius norm between the two matrices)

$$\mathcal{E}^{(2)} \equiv \frac{2}{N_v(N_v - 1)} \sum_{i < j} (C_{ij}^{\text{RBM}} - C_{ij}^{\mathcal{D}})^2. \quad (3)$$

1.4 Error of the third moment

Similarly, we can compute the MSE of the third moment of the data representation sites $C_{ijk} = \overline{(v_i - m_i)(v_j - m_j)(v_k - m_k)}$, with $m_i = \bar{v}_i$. We will refer to this error as $\mathcal{E}^{(3)}$ and it was not shown in the main-text. Since the number of moments scales as $\sim \mathcal{O}(N_v^3)$, we shall focus only on the most active sites: the ones where the empirical frequency m_i is as close as possible to 0.5. In practice, we took the 50 more active sites. The expression is given by

$$\mathcal{E}^{(3)} = \frac{6}{N_v(N_v - 1)(N_v - 2)} \sum_{i < j < k} (C_{ijk}^{\text{RBM}} - C_{ijk}^{\mathcal{D}})^2. \quad (4)$$

1.5 Power spectrum density

For images, we compute the average power spectrum at fixed distance r of both a set of generated images and of the original dataset. In practice, we compute the logarithm of the module of the Fourier coefficient at a fixed distance d in Fourier space

$$P(d) = \log (\langle \|A_{kl}\|^2 \rangle_{(k,l)|k^2+l^2=d^2}), \quad (5)$$

where A_{kl} are the image’s discrete 2D Fourier transform elements. Again, we compare the values obtained with the generated dataset with those of the real dataset through the MSE. We will refer to this error as \mathcal{E}^{PSD} which is defined as:

$$\mathcal{E}^{\text{PSD}} = \sum_d [P(d)^{\text{RBM}} - P(d)^{\mathcal{D}}]^2. \quad (6)$$

1.6 Adversarial Accuracy Indicator

A recent indicator has been introduced in Ref. [3] for measuring the resemblance and the “privacy” of data drawn from a generative model with respect to the training set that has been used to train the model. This metric is based on the idea of data nearest neighbors. We begin by defining two sets containing each one N_s samples: (i) a “target” set containing only generated samples $T \equiv \{\mathbf{s}_{\text{RBM}}^{(m)}\}_{m=1}^{N_s}$ and (ii) a “source” set containing only samples from the dataset $S \equiv \{\mathbf{s}_{\mathcal{D}}^{(m)}\}_{m=1}^{N_s}$. Then, for each sample m in T , we compute the minimum euclidean distance to a sample in S , that is $d_{TS}(m) = \min_n \|\mathbf{s}_{\text{RBM}}^{(m)} - \mathbf{s}_{\mathcal{D}}^{(n)}\|$. In other words, we look for the “nearest neighbor” of our generated sample in the original dataset. We can do exactly the same calculation the other way around, and look for the generated sample that resembles more to a sample in the original set, and compute $d_{ST}(m)$. Finally, we can also measure the minimum distance from a sample m to a different sample in the same set, thus obtaining $d_{SS}(m)$ and $d_{TT}(m)$. Once having all these 4 distances, we can estimate the frequency at which we find the nearest neighbors of a data point in the same set that already contained that point, that is

$$\mathcal{A}_S = \frac{1}{N_s} \sum_m^{N_s} \mathbf{1}(d_{SS}(m) < d_{ST}(m)) \quad \text{and} \quad \mathcal{A}_T = \frac{1}{N_s} \sum_m^{N_s} \mathbf{1}(d_{TT}(m) < d_{TS}(m)). \quad (7)$$

It is clear that if the generated samples were statistically indistinguishable from real ones, these two measures should converge to the value of a random guess 0.5 when $N_s \rightarrow \infty$. Furthermore, \mathcal{A}_S close to 1 means that the generated samples are very dissimilar to the true ones while, if close to zero, means that the generated samples are that close to the true ones that we are overfitting the dataset. On the other way around, whenever \mathcal{A}_T is close to one, we can affirm that the generated samples are all very close to each others, which can be related to a lack of diversity in the target set or because the generated samples are very far away from the true ones. If close to zero, it reflects again overfitting. In the main text article, for simplicity, we use the MSE estimate of the two indicators:

$$\mathcal{E}^{\text{AA}} \equiv (\mathcal{A}_S - 0.5)^2 + (\mathcal{A}_T - 0.5)^2. \quad (8)$$

1.7 Entropy

Our last indicator to compare the true and the generated datasets is the entropy. Here, we will approximate the entropy of a given set of data by its byte size when compressed using `gzip`. We therefore define the entropy of N_s samples from the true dataset as S_{src} and we compare it to the entropy of a set of the same size where half of the samples are drawn from the true dataset while the other half is taken from the generated configurations. We refer to this entropy as the cross entropy S_{cross} . We compare these 2 quantities through

$$\Delta S = \frac{S_{\text{cross}}}{S_{\text{src}}} - 1 \quad (9)$$

When ΔS is large, it means that the generated samples are less “ordered” than the samples coming from the source. On the contrary, if small, it means that the generated samples lack diversity (as compared to the original dataset).

1.8 Frechet Inception Distance score

For image datasets, we can also use other typical estimators such as the Frechet Inception Distance score (FID) [4]. The FID metric compares the distribution of the activation variables of a neural network (typically Inception v3 trained on the ImageNet) when fed with real or generated images. As we show in Figs. 4 and Fig. 19, this estimator behaves qualitatively in the same way than the estimators discussed in the main-text.

2 Details of the RBM used for the training of MNIST

2.1 RBMs details

All the RBMs that have been used to learned the MNIST dataset have been trained with the following parameters. First of all, only the first 10000 images of MNIST where used, threshold (for the mapping to black/white) at the value 0.5. The test set consisted of 1000 other images. Parameters of the network and learning procedure:

- Number of hidden nodes: $N_h = 500$.
- Learning rate: $\alpha = 0.01$.
- Minibatch size: $n_{mb} = 500$.
- No ℓ_2 regularization of momentum.
- The gradient is centered according to Ref.[5].
- The visible biases are initialized to match the empirical frequency of the training dataset:

$$\eta_i = \log \left(\frac{\bar{m}_i}{1 - \bar{m}_i} \right) \text{ where } \bar{m}_i = \frac{1}{M} \sum_m s_i^{(m)}. \quad (10)$$

- The number of Markov chains used to estimate the negative term of the gradient was always equal to n_{mb} .
- The number of MCMC steps used for the negative chains is indicated by the variable k , and vary in the different experiments.
- For the indicators, we used $N_s = 1000$ samples.

2.2 Computer load

All the RBM’s trainings were done on NVIDIA GPU RTX 3090, using the pytorch library [6]. The runtime in MNIST ranges from less than an hour when $k = 10$ to ~ 2 days when $k = 10^4$, for reaching a number of updates $t_{\text{age}} = 200000$. The generation sampling of new configurations is done on CPU (Intel(R) Xeon(R) @ 2.60GHz). Typical analysis were several minutes long for each t_{age} , which the exception of the time auto-correlation functions that required some few hours to complete.

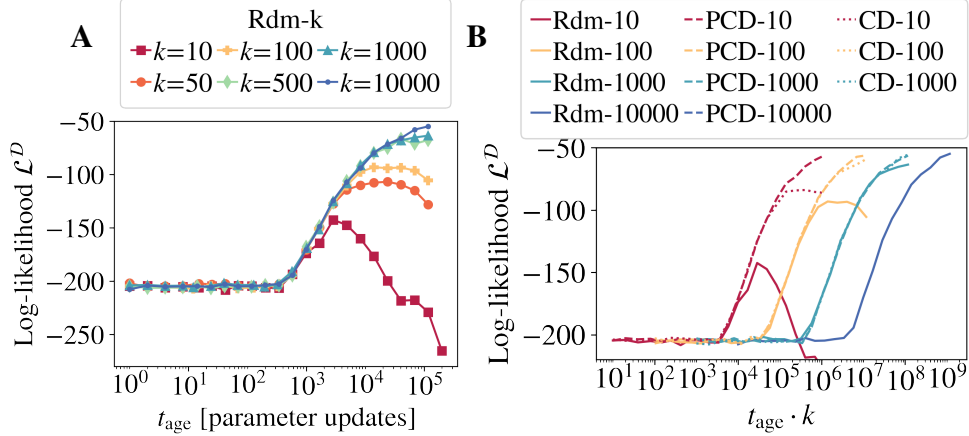


Figure 1: Evolution of the log-likelihood (LL) on the dataset along the learning. In **A** we show the LL measured during the training of RBMs with the Rdm- k scheme, as function of the number of parameters updates, t_{age} . We include data for RBMs trained with different values of k . In **B** we compare (for several values of k) the LL obtained with different schemes as function of the product $t_{\text{age}} \cdot k$, which is proportional to the total learning time.

3 Additional results for MNIST

3.1 Rdm- k scheme

We show the evolution of LL on the dataset during the learning process using the Rdm- k scheme for different values of k in fig. 1-A, and compared with other training schemes in fig. 1-B.

We illustrate on the fig. 2 the samples that we obtain at different sampling times, t_G , for the older RBM we have trained with the Rdm-100 scheme.

We clearly see that during the learning process, the RBM memorized in its structure the dynamics followed to train it, and that the equilibrium configurations do not match the dataset density distribution. We stress here that the number of MCMC steps used to estimate the negative term of the LL gradient, k , is rather large in this case ($k = 100$, for sure larger than the common values used in the literature) and yet, we start to observe out-of-equilibrium effects quite quickly during the learning.

We show on fig. 3 and fig. 4 the evolution of the quality observables measured during the sampling stage for various values of k . As described in the main-text: when k is small in comparison to the mixing time the system enters quickly in the OOE regime, developing a peak of performance at $t_G \sim k$. For the case $k = 100$, we show in fig. 5, the evolution of the position of this peak (its position in the time axis in fig. 5-A and its height in fig. 5-B) with the RBM's age. We can see that the position of the best quality peak converges quite early to $t_G \sim k$, but the overall quality of the generated samples at that time continues improving with the number of parameter updates during the training even if the LL of the dataset, \mathcal{L}^D , does not improve anymore at these values of t_{age} , as is shown in fig. 1. Furthermore, the quality of the generated samples at this peak does not change much with the value of k used to estimate the negative term of the gradient, as shown in fig. 6-A. And not only, already with some few k steps, we can generate samples that are much better than those generated with CD- k or PCD- k using much larger values of k (see fig. 6-B).

We further compare the evolution of the quality estimator \mathcal{E}^{PSD} along 2 sampling runs initialized either at random or at the dataset in fig. 7. We highlight the time, t^{therm} , at which both simulations converge to the equilibrium value. These are the times that were plotted as function of t_{age} in fig.3-C in the main-text.

3.2 Relaxations of equilibrium and OOE models

In the main-text, the mixing times were estimated through the equilibrium magnetization time-autocorrelation function $\rho(t)$. At that point, we mentioned that we could only properly estimate

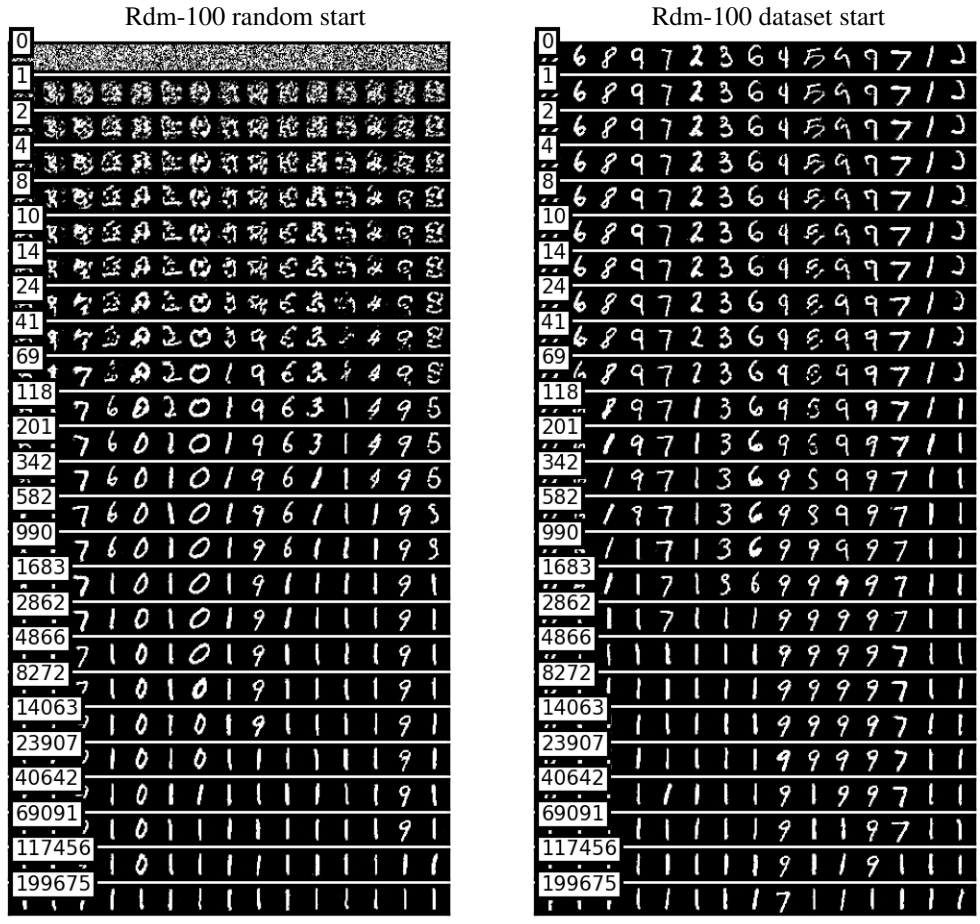


Figure 2: We show some examples of the images we generate at different steps of the data generation sampling of an RBM trained with the Rdm-100 scheme for $t_{\text{age}} = 199876$ parameter updates. Samples generated at the same number of MCMC steps are grouped together in rows and the value of t_G is given in the top left corner of each row. Runs initialized at random configurations are shown on the left panel, and on the dataset on the right. Each column follows the evolution of a Markov chain initialized from random or from the dataset and iterated for almost 200000 steps. We see that at $t_G = 118 \sim k = 100$, we obtain nice samples having a fair representation of all digits. For lower number of MCMC steps, the chain didn't converge yet to numbers (in the case of random initialization) and, for longer ones, almost all samples are vertical ones (for both kinds of initialization) which clearly dominate the learned equilibrium distribution.

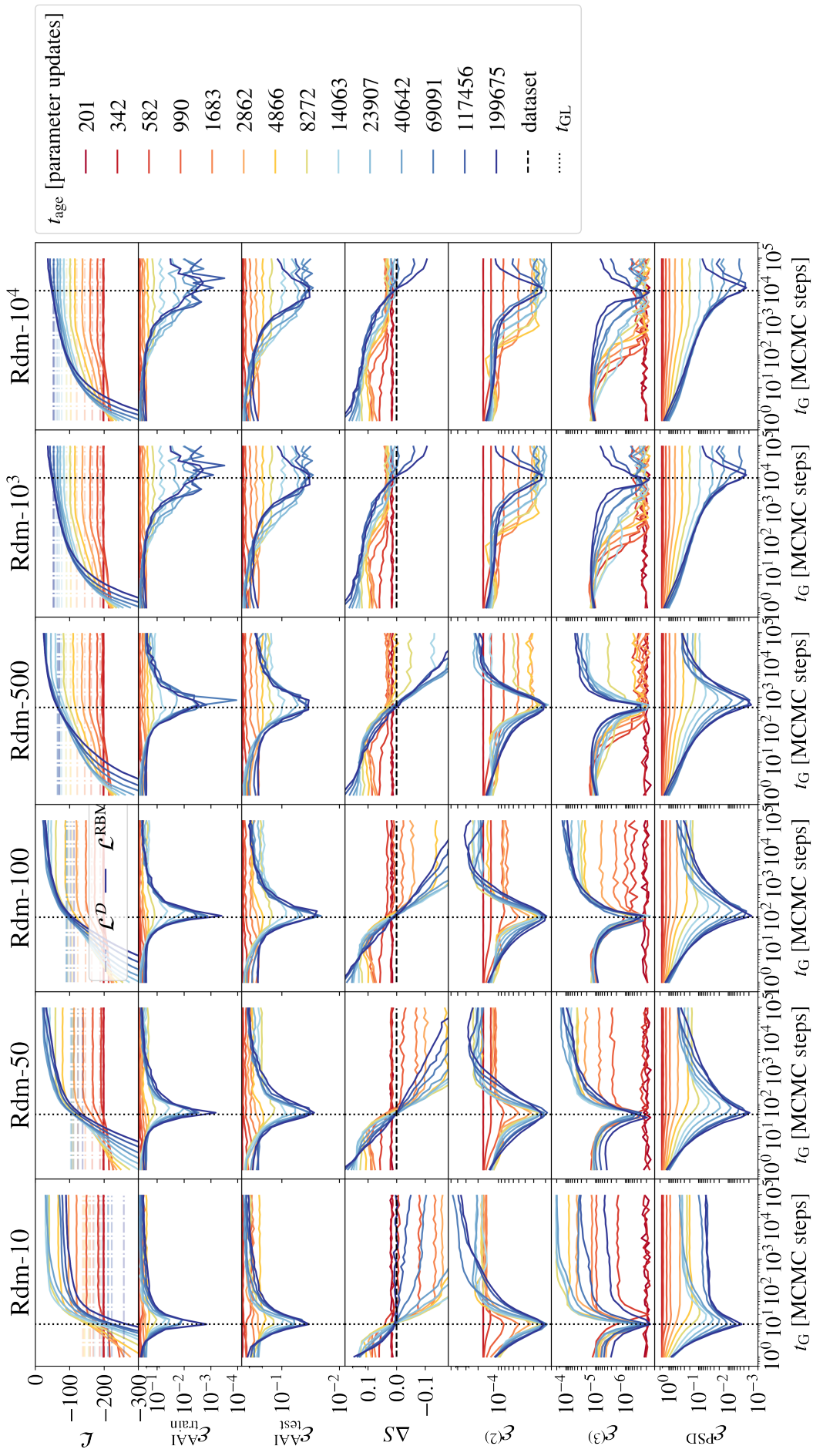


Figure 3: Evolution of the quality estimators along the sample generation for MNIST database for RBMs trained using the Rdm-k approach and with different values of k . For the case of the \mathcal{E}^{AAI} estimator, we have shown both the results obtained when comparing with the training ($\mathcal{E}^{\text{AAI}}_{\text{train}}$) or the test set ($\mathcal{E}^{\text{AAI}}_{\text{test}}$).

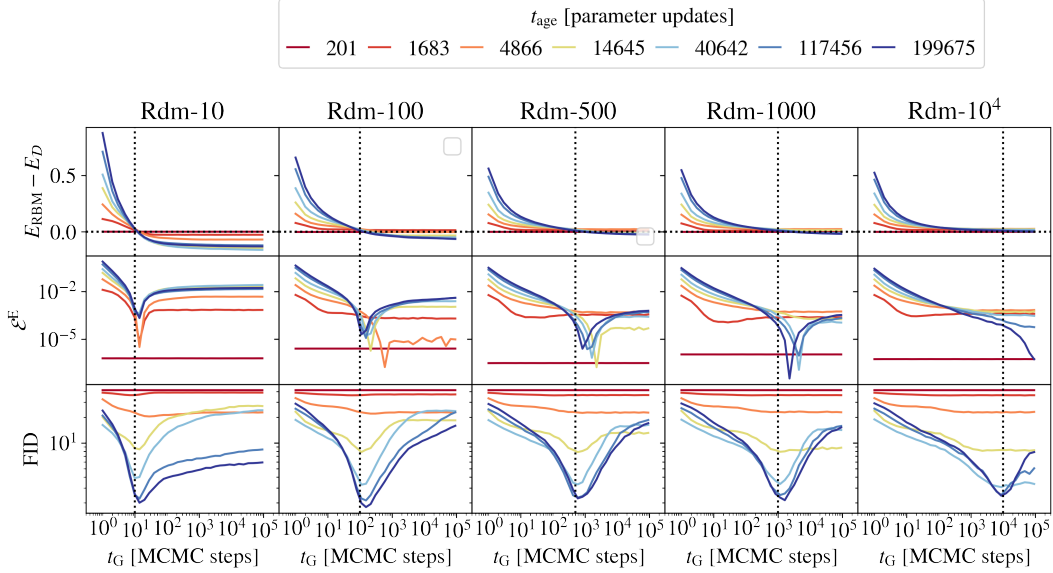


Figure 4: We show some extra estimators of the generated sample quality as function of the sampling time: the energy of the generated E_{RBM} and original $E_{\mathcal{D}}$ datasets, the error in the energy \mathcal{E}^E , and the FID score.

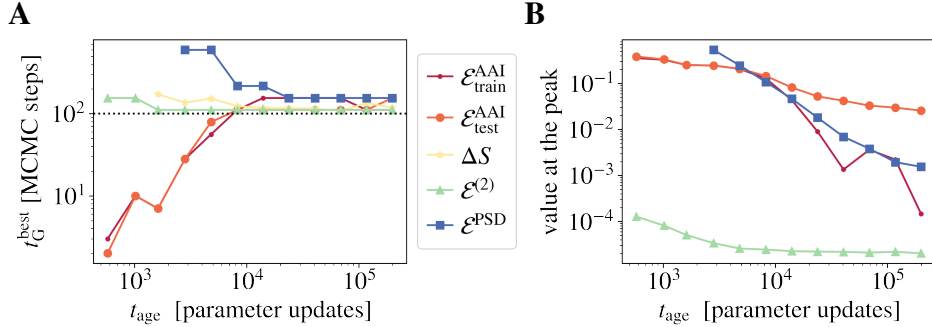


Figure 5: For RBMs trained with the Rdm-100 scheme, we show in **A**, the sampling time t_G at which we observe the best generation performance in the estimators shown in fig. 3 (that is, the position of the “best quality peak”), as function of the age of the RBM. In **B** we show the value reached by these estimators at the times shown in **A**, also versus the t_{age} .

it in the $k = 10^4$ RBMs because poorly trained RBMs displayed extremely slow dynamics. In fact, these very slow relaxations prevented us to thermalize the system for most of the t_{age} studied in the low k models. We can further elaborate this argument by studying the relaxations from configurations at different times. In particular, we consider two different RBMs (both trained with the Rdm- k scheme for the same number of updates $t_{\text{age}} = 40620$): one using $k = 10$ and the other with $k = 10000$. Indeed, at that age, the Rdm-10000 RBM has learned the equilibrium model and the Rdm-10 RBM encodes a strongly OOE model, as discussed in the main-text. In order to characterize the relaxations of both models, we recompute the time-autocorrelation function discussed in the main-text. However, this time, we explicitly compare the magnetization at time $t + t_w$, with the magnetizations at time t_w ,

$$\rho(t, t_w) = \frac{C_m(t, t_w)}{C_m(t_w)}, \text{ where } C_m(t) = \frac{1}{N_v} \sum_i (m_i(t + t_w) - \bar{m}_i)(m_i(t_w) - \bar{m}_i) \quad (11)$$

We refer to t_w as the “waiting” time. Clearly, equilibrium is reached when $\rho(t, t_w)$ does not depend on t_w anymore. We show in fig.8-A and B, the relaxations of the Rdm-10 and Rdm-10000 models, respectively. Clearly, the relaxations of the Rdm-10 model are far slower than those of the Rdm-

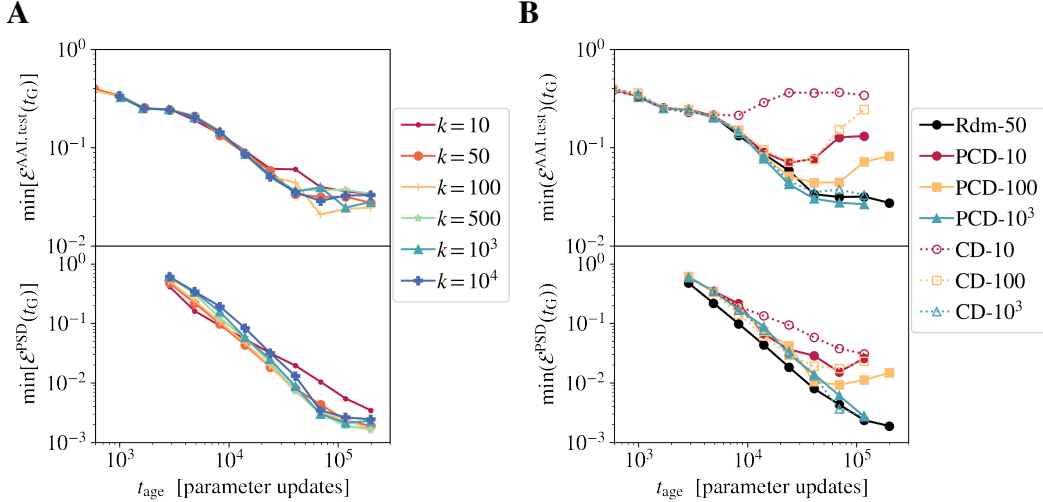


Figure 6: **A** We show the height of the best performance peak (for RBMs trained with the Rdm- k scheme) for the \mathcal{E}^{AAI} (on the test set) and \mathcal{E}^{PSD} estimators, as function of the machine’s age for different values of k (the same curves were already shown in fig. 5 in the case $k = 100$). We observe so little improvement of the generative performance with k at the best performance peak. In **B**, we show the minimum of the values measured for these two estimators during the sampling of RBMs trained with the CD- k (dashed lines and empty symbols) and PCD- k (continuous lines and full symbols) scheme as function of t_{age} and for several values of k . In this case, the quality of the generated samples improves notably with k and even worsen over t_{age} (something not observed in the Rdm scheme). For the sake of comparison, we also show the values obtained with the Rdm-50 scheme (in black, already shown in **A**), displaying remarkable better generation performances only comparable with the RBMs trained with $k = 1000$.

10000. Showing the former, actually, forever aging effects extremely similar to those observed in spin glasses.

3.3 CD- k scheme

In the CD case on fig. 10, we see that for small k , the system enters quickly in the OOE regime. However in that case, the interaction between the initial condition and the dynamics lead to a behavior hard to predict: the peak of best performance, if it exists, moves with the age of the machine, and the general performance are not good. When $k = 1000$ we observe quite a good performance. This is due to the fact that at the beginning of the learning this number of MCMC steps is sufficiently high to decorrelate from the initial condition. As t_{age} increases, the dataset is presumably a better initial condition than taking a random one, and the length of the MC chain is probably enough to thermalise correctly. This agrees with the fact that $k = 1000$ is comparable to the highest values of the mixing time t_α shown in the main-text. We should still remark that in that case, t_G needs to be very large if one wants to generate equilibrium configurations during the sampling.

In fig. 9 we illustrate the behavior of CD-100 both when sampling using the dataset as initial condition or starting from random ones. It is clear that the configurations visited when starting from random almost never reach a digit (even with $k = 100$). When initialized at the dataset, and as explained before, the system explore nearby configurations (we can see that the chains do not decorrelate from the original digit) until it manages forget the initial configuration and starts to sample spurious states (which are definitely not numbers).

3.4 PCD- k scheme

Let us finish with the PCD case. We give a glance of the sample generation process of a RBM trained with PCD-100 in fig. 12. We have considered two possible starts for the MC chain: random and dataset, and for both cases, it seems clear that we need at least 10000 sampling MCMC steps to start to sample good digits that are also uncorrelated initialization of the chains. We quantify these

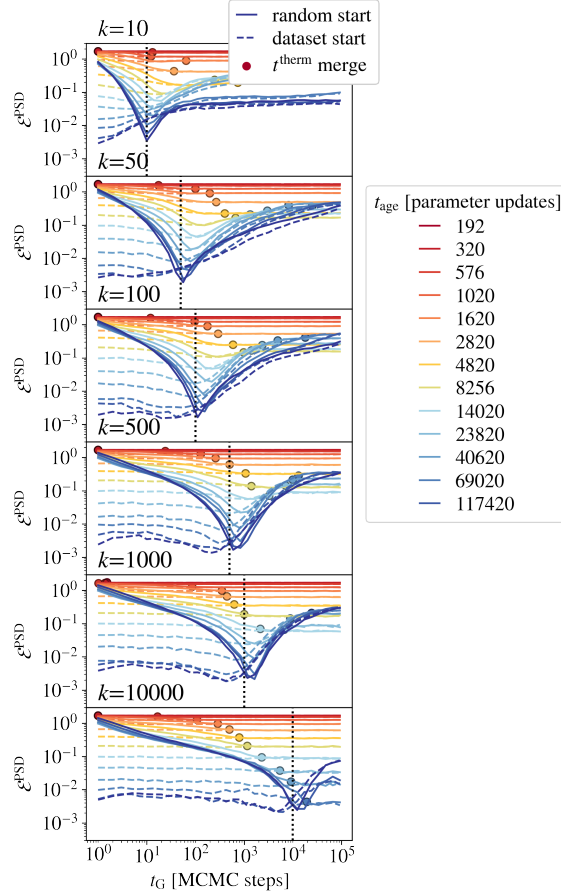


Figure 7: Evolution of \mathcal{E}^{PSD} during the sampling of RBMs trained with MNIST data and with the Rdm- k scheme for different values of k (different cells) and different t_{ages} (coded by colors). In continuous lines, we show the measures obtained with runs initialized at random, and in dashed lines, those from runs initialized at the dataset. We highlight with a circle, the point at which both measures merge to the same constant curve. The $k = 10^4$ curve was included in fig. 3-B of the main-text.

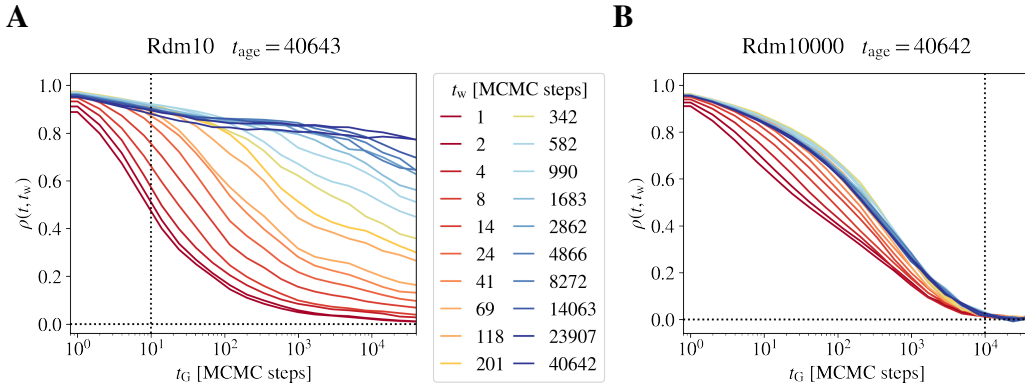


Figure 8: We show the two-time-autocorrelation function of the magnetizations, $\rho(t, t_w)$, defined in Eq. 11, during the sampling of two RBMs: either trained with Rdm-10 (in **A**) or Rdm-10000 (in **B**). Both RBMs were trained for a fixed number of updates $t_{\text{age}} = 40642$ (or 40643) and we code by colors the value of the waiting time t_w used to compute $\rho(t, t_w)$. In **A**, the longer we wait, the slower the relaxation for all the t_w considered. In **B**, curves above $t_w > 500$ converge to the same relaxational curve, which coincides with the one showed for that age in fig.3-A of the main-text.

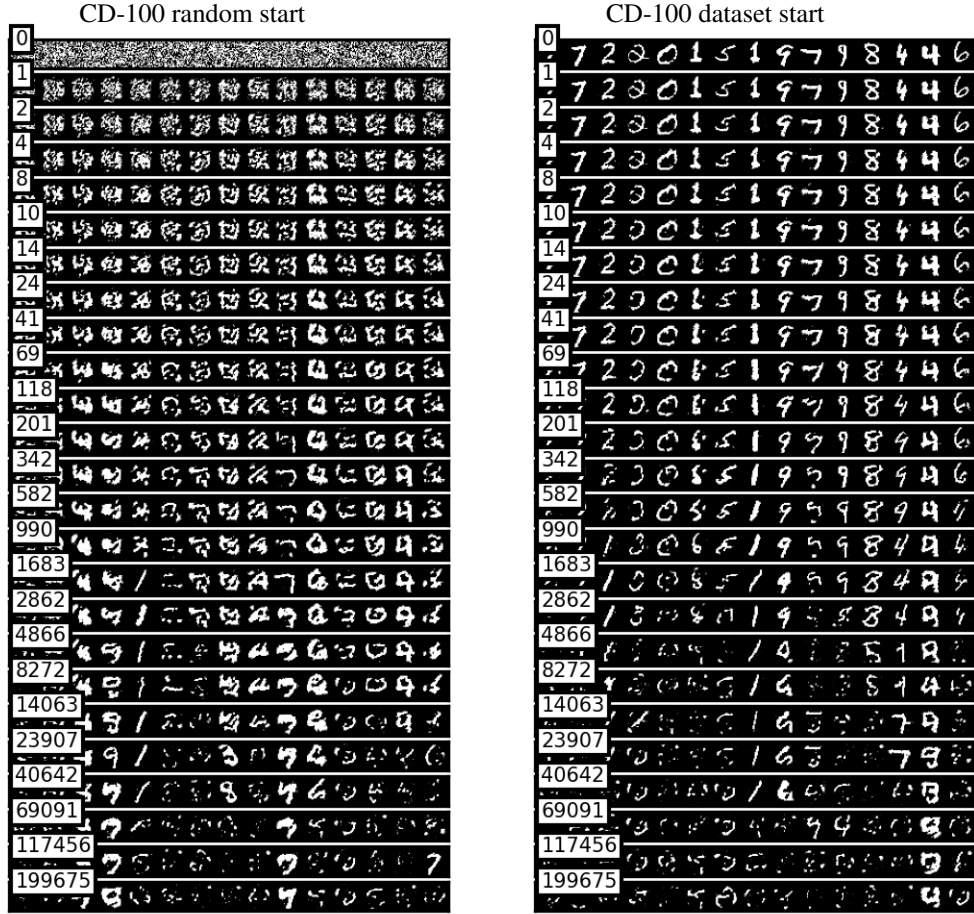


Figure 9: Same experiment shown in fig. 2, but this time sampling an RBM trained with the CD-100 scheme for $t_{\text{age}} = 199876$ parameter updates. Even with $k = 100$, RBMs trained with the CD- k scheme are not able to create digits from scratch, as shown in the random initialization Markov chains. If instead, the chains are initialized at the dataset, they remain close to the original digit for at least $t \sim 3000$ MCMC steps, without decorrelating from the initial condition. For larger times, the machine does not generate digits anymore.

observations by looking at the evolution of the quality observables with the sampling time (see fig. 11). In this case, the PCD approximation scheme does a good job, the permanent chain manages to keep the RBM at quasi-equilibrium during all the learning, which is consistent with the observation that RBM’s parameters change really slowly during the learning. In fact, we see almost no memory effects in the dynamics, even for small k . Yet, it is important to remark that the time needed to obtain equilibrated samples from scratch is quite high. In addition, the quality of the best generated samples using this training scheme are significantly worse than those obtained in the OOE regime of Rdm- k . Also the AAI score on the test set is not as good as for the Rdm- k scheme unless we reach MCMC chains of $k = 1000$, as shown in fig. 6-B.

3.5 Comparisons between different training schemes

We have shown that different training schemes generate RBMs that display different generation sampling dynamics (when trying to create digits from scratch just through the sampling of their Gibbs equilibrium distribution). Indeed, the evolution of the quality estimators for Rdm- k , CD- k and PCD- k are shown in Figs. 3, 10 and 11 respectively. For the Rdm case, we see that that by increasing k we reach equilibrium for larger t_{age} , but eventually we end up in the OOE regime as the mixing time keeps increasing with the number of LL gradient updates. For CD, it seems that for $k = 10, 100$, the RBM enters in an uncontrolled OOE regime, while when $k = 1000$, the machine

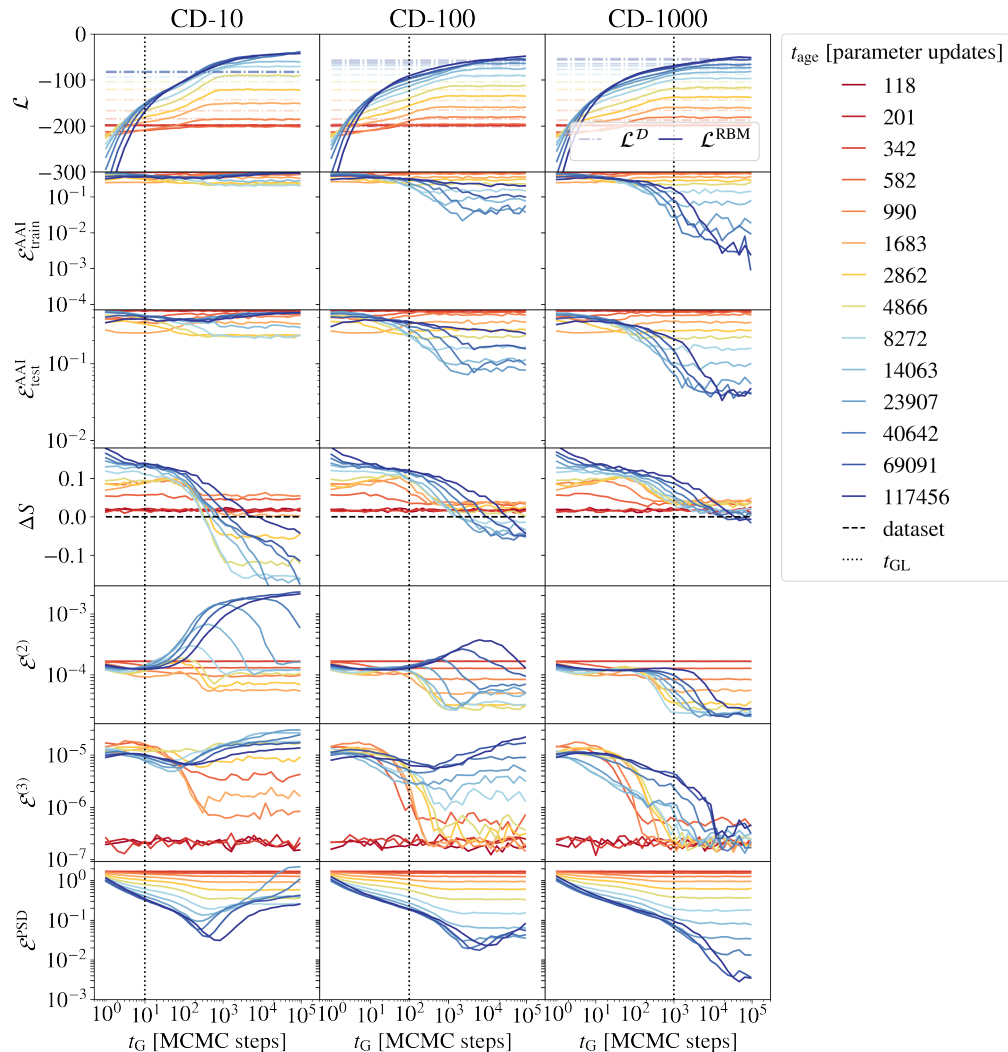


Figure 10: Evolution of the quality estimators along the sample generation for MNIST database for RBMs trained using the CD- k approach and with different values of k .

seems to have a nice equilibrium behavior (to confirm such behavior one should quantify the mixing time). Finally, in PCD, when $k \geq 100$ we observe that the machine ends up in a good equilibrium regime where the quality of the generated samples increase with k . Again, the mixing time should be controlled to confirm this conclusion. Still, we can also observe that the best generation performance is not necessarily reached on this equilibrium regime. Indeed, we can observe in fig. 6 that RBMs running on the OOE regime generates far better samples than CD or PCD for short values of k , and very similar for large k . In fact, in fig. 6-B, we show the minimum value measured in two quality estimators as function of t_{age} for the different schemes, showing that the Rdm-50 runs create samples as good as PCD-1000 ones at long t_{age} (despite being the training of the former 20 times faster). For shorter values of t_{age} , the quality of the samples generated by the Rdm-50 RBMs, always that of overpasses CD or PCD-1000.

4 Results for a Human Genome dataset

In this case we considered the population genetics' dataset of Ref. [7]. This dataset corresponds to a sub-part of the genome of a population of 5008 individuals, for which the alteration or not of a given gene is indicated by a $\{0, 1\}$ variable. A total of 805 genes are reported. For our study, the

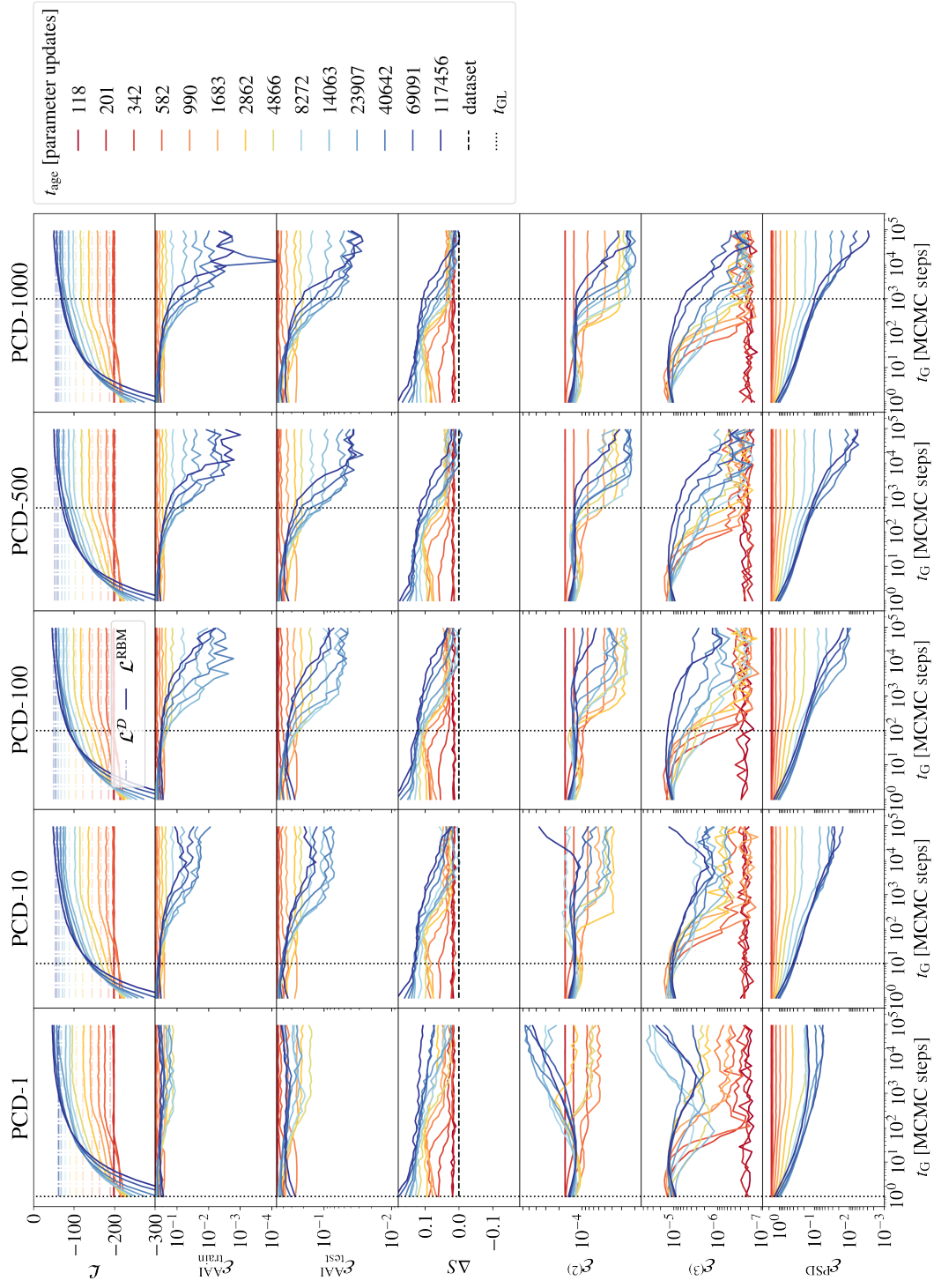


Figure 11: Evolution of the quality estimators along the sample generation for MNIST database for RBMs trained using the PCD-k approach and for different values of k .

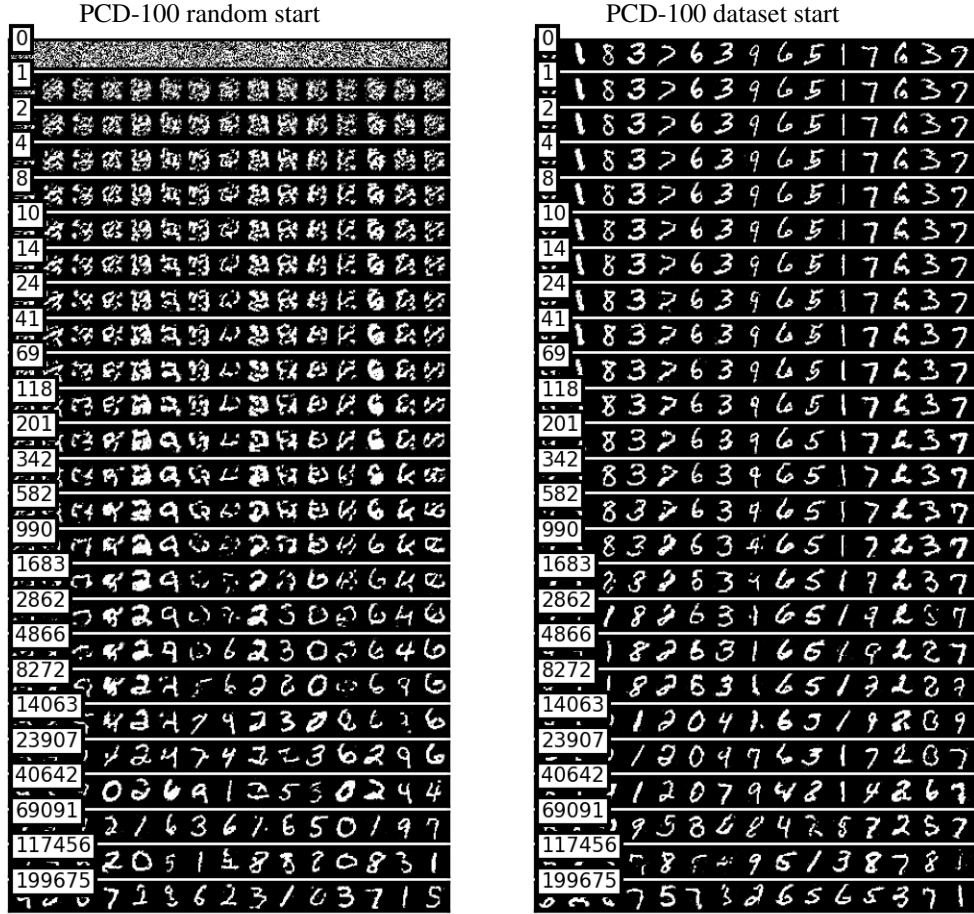


Figure 12: We show some examples of the images we obtain at different steps during the data generation sampling of an RBM trained with the PCD-100 scheme for $t_{\text{age}} = 199876$ parameter updates following the same procedure discussed in fig. 9.

dataset was separated into 4500 samples for the train set and 500 for the test set. For this dataset, the following parameters of the RBM were used:

- Number of hidden nodes: $N_h = 100$
- Learning rate: $\alpha = 0.01$
- Minibatch size: $n_{mb} = 250$
- For the indicators, we used all the training set $N_s = 4500$ (and only 500 for measurement involving the test set).
- the rest is the same as for MNIST.

We observe for this dataset qualitatively the same behavior as for MNIST. We show on fig. 13 a figure similar to fig. 3 in the main text for this dataset. We observe, again, two clear regimes: the equilibrium and the OOE. The equilibrium regime is observed for almost all the RBMs trained with $t_{\text{age}} \lesssim 3000$ updates (except for the Rdm-10 RBM), and the OOE regime, for older machines. It is quite remarkable that the samples generated by RBMs of age $t_{\text{age}} = 2862$, reproduce quite well the dataset's 2 and 3 points-correlations (as shown in the $\mathcal{E}^{(2)}$ and the $\mathcal{E}^{(3)}$ observables), but display quite poor values for \mathcal{E}^{AAI} . The fact that all the RBMs with $k > 10$ reproduce essentially the same curves with time, tells us that the relaxation time is rather low below this age, surely over 10 MCMC steps and below 50. However, beyond this age, the mixing time grows drastically, clearly overpassing the 10^4 steps since none of our RBMs describe the equilibrium dynamics for any of the blue lines. Yet, even in the OOE regime, we are still able to generate very good samples (as reflected

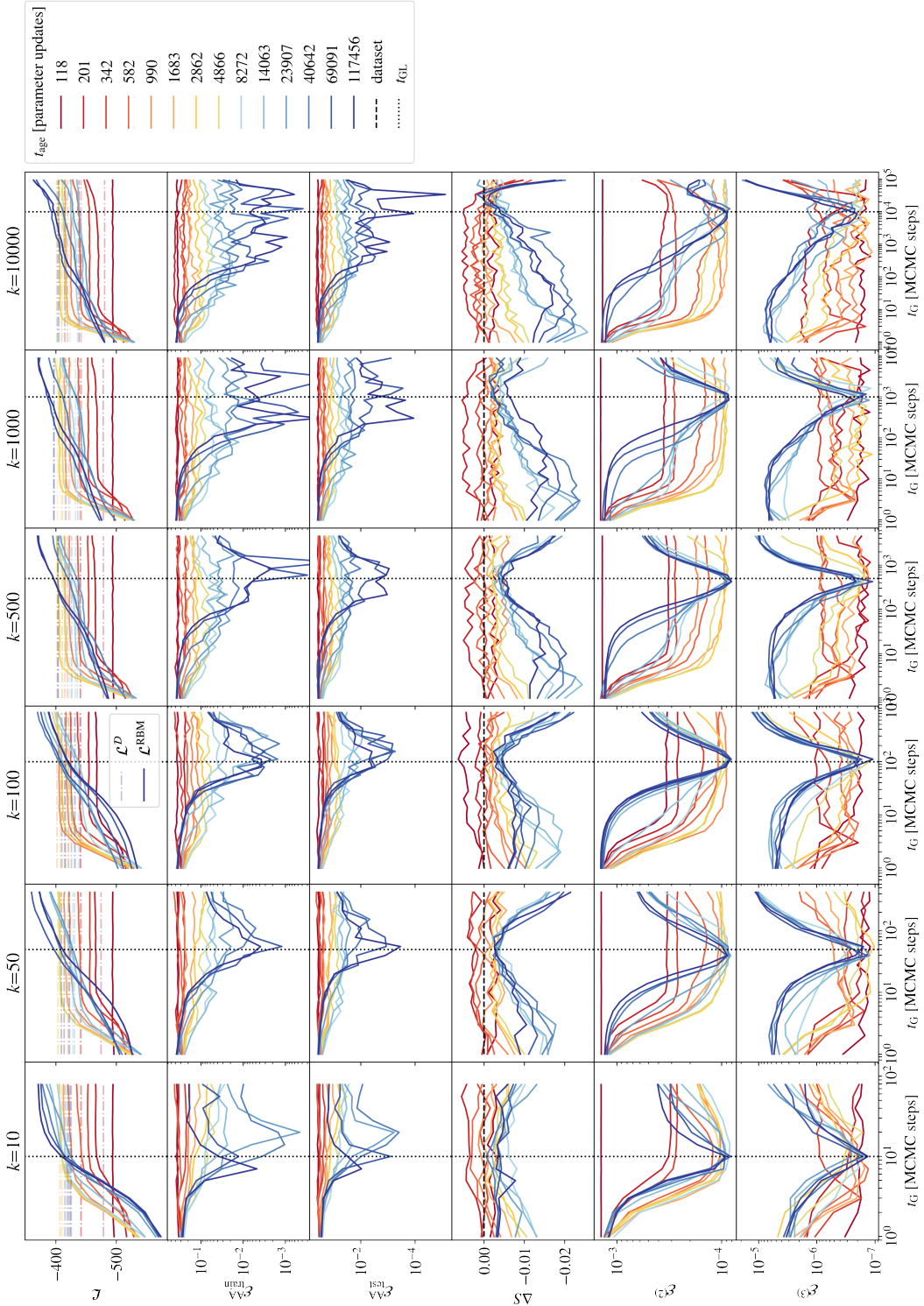


Figure 13: Evolution of the quality estimators during the sampling of the dataset of population genetics for RBMs trained using the Rdm scheme and for various values of $k = 10, 50, 100, 500, 1000, 10000$. We clearly see the same behavior where the best performance are obtained for $t_G \sim k$. The system never manage to equilibrate, even for $k = 10000$.

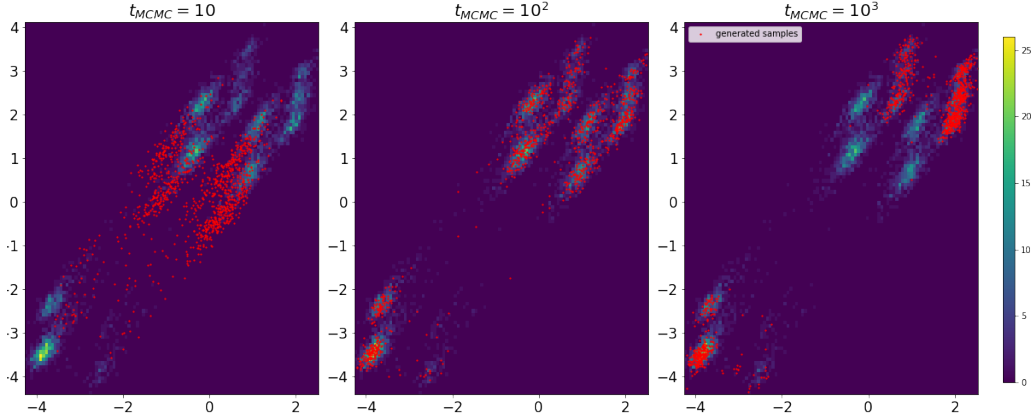


Figure 14: All three images: histogram (as heatmap) of the scatter plot along the first two eigenvectors of w of the dataset. From left to right: the red dots correspond to the scatter plot of 1000 samples generated by the RBM at respectively at $t_G = 10, 10^2, 10^3$ Monte Carlo steps. The RBM has been trained using the Rdm-100 scheme, and the best match between the projections of the original and generated dataset are observed precisely at $t_G \sim k = 100$.

in all the quality observables) as long as we limit the generation sampling to $t_G \sim k$ MCMC steps for each RBM (just as observed in the MNIST’s case).

Finally, we believe that this sudden and brutal growth of the mixing time with t_{age} is related to the structure of this dataset: the MCMC simulations get trapped in some relative maxima of the LL, and it takes extremely large times to escape from them. To illustrate this, we can project the samples either on the first principal directions or, on the left-eigenvectors of w_{ia} as discussed in [8]. We show in fig. 14, the projection of the dataset along the directions of the first two eigenvectors of the dataset (being each the horizontal and vertical axis, respectively), and the projection of the generated samples at 3 different sampling times. The original dataset is shown as a heatmap of the point density, and the generated dataset as red dots. We clearly show that at $t_G = k$, the generated samples provide a very good cover of the dataset density. At the opposite, after very few updates, it didn’t spread correctly, and after too many updates, the samples cluster into a small subset of the data density distribution.

5 Results for CelebA

This dataset corresponds to a total of 30000 faces of celebrity, in color and potentially in high-resolution. In our case, we first downsized the dataset to a resolution of 128×128 in order to reduce the computational time of the learning part. Since RBM are more suited to handle binary entries, we then clipped the images’s pixels at a value of 0.3. For our study, we only considere a train set of 30000 samples. For this dataset, the following parameters of the RBM were used:

- Number of hidden nodes: $N_h = 5000$
- Learning rate: $\alpha = 0.01$
- Minibatch size: $n_{mb} = 500$
- For the indicators, we used $N_s = 1000$ samples.
- the rest is the same as for MNIST.

We observe for this dataset qualitatively the same behavior as for MNIST, even though it is clearly much harder to learn. Due to the learning time, we will show only the results for $k = 50, 100, 500$. We show on fig. 15 the evolution of the sampling for our indicators and for many values of t_{age} . We also show on fig 16 sampling obtained for thr Rdm-100 machine for several values of t_G , demonstrating the RBM can indeed learn quite complex dataset.

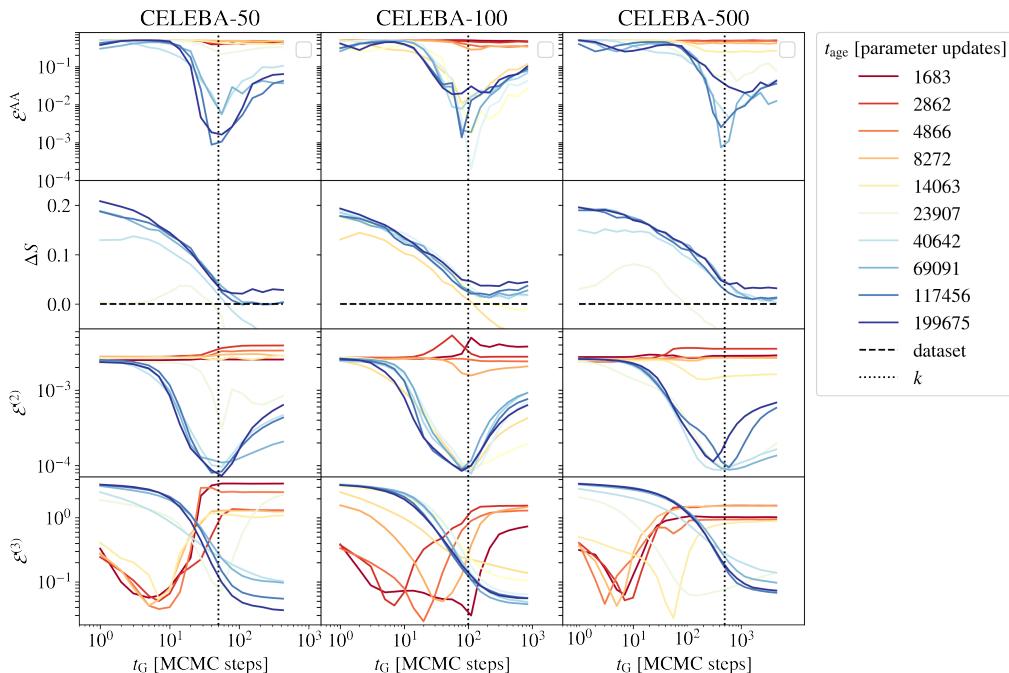


Figure 15: Evolution of the quality estimators during the generation sampling of CELEBA images, for RBMs of different ages (t_{age} coded by colors), and trained using the Rdm- k scheme with $k = 50, 100$ and 500 in different columns. The best generation performance is also observed clearly around $t_G \sim k$, except for the PSD observable which is not able to characterize properly these kinds of images. For this case, we remove the indicator on the third moment since it was too computationally demanding.

6 Results for FashionMNIST

The FashionMNIST[9] dataset corresponds to a total of 60000 images of 28×28 pixels in grayscale. The dataset represents various classes of clothers (shirts, pants, ...). For this dataset, we train the RBM on input rescaled within $[0, 1]$ but we didn't discretize the values as we did for MNIST. The following parameters were used for the training:

- Number of hidden nodes: $N_h = 1000$
- Learning rate: $\alpha = 0.01$
- Minibatch size: $n_{mb} = 500$
- For the indicators, we used $N_s = 1000$ samples.
- During the training we used $k = 100$ Gibbs steps.
- the rest is the same as for MNIST.

We show on fig. 17 a subset of the dataset together with the generated images of the RBM. Then, we show on fig. 19 the results of several indicators for this case, showing again the characteristic non-equilibrium best-performance peak around $t_G \approx k$. Finally, we show visually how the generated images evolve with the sampling time, up to a very long number of MCMC steps in fig. 18.

7 Results for Caltech101 Silhouettes

This dataset corresponds to a total of 8671 images of 28×28 pixels in black and one, corresponding to the silhouette of various objects.. The dataset is made of binary input from which not pre-treatment was made. The following parameters were used for the training:

- Number of hidden nodes: $N_h = 500$



Figure 16: Faces generated by the RBMs starting from random initial conditions, trained with Rdm-100 and up to $t_{\text{age}} = 360000$. Each row represent a fixed number of sampling steps. We can see at the beginning that very quickly the MC chains is able to generate very blurry faces. Then, when $t_G \sim O(100)$ it generates quite decent faces. Later, the chains seem to be biased toward more obscure version of the faces.

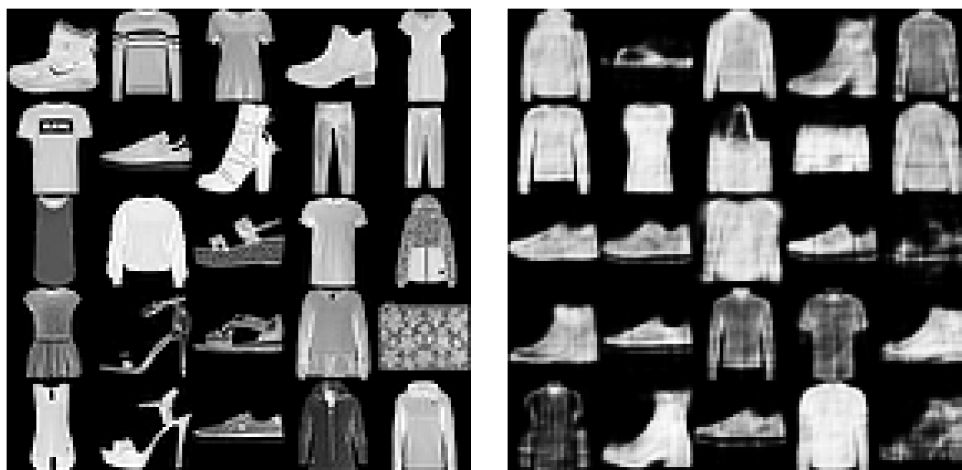


Figure 17: **Left:** A subset of FashionMNIST showing 25 random samples. **Right:** 25 images generated from the RBM trained of the FMNIST dataset. The RBM was trained up to $t_{\text{age}} = 200k$ and extracted at $t_G = k = 100$

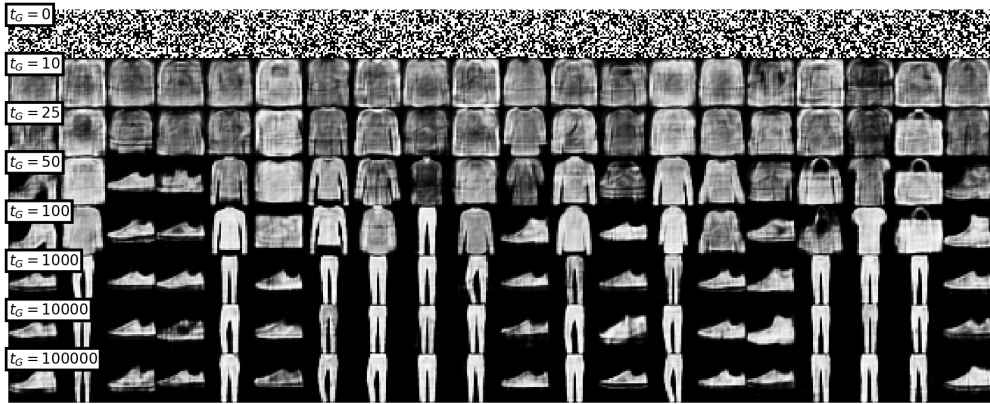


Figure 18: Various samples obtained from the RBM at different values of t_G . We see that when $t_G = k$ we obtain quite good samples while for large sampling time the generated images over-represent pants and shoes.

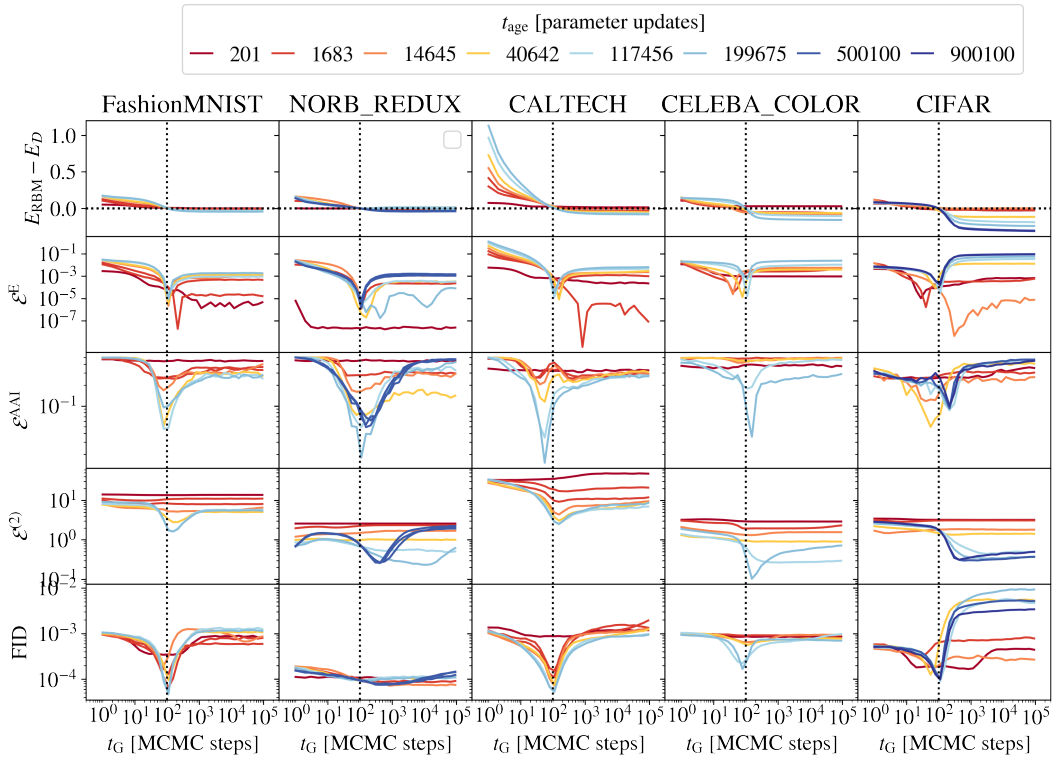


Figure 19: We show the evolution of several quality estimators for RBMs trained with $k = 100$ in 5 different datasets: FashionMNIST, NORB REDUX, CALTECH101 Silhouettes, CELEBA in colour and CIFAR. Each dataset is shown in a different column.

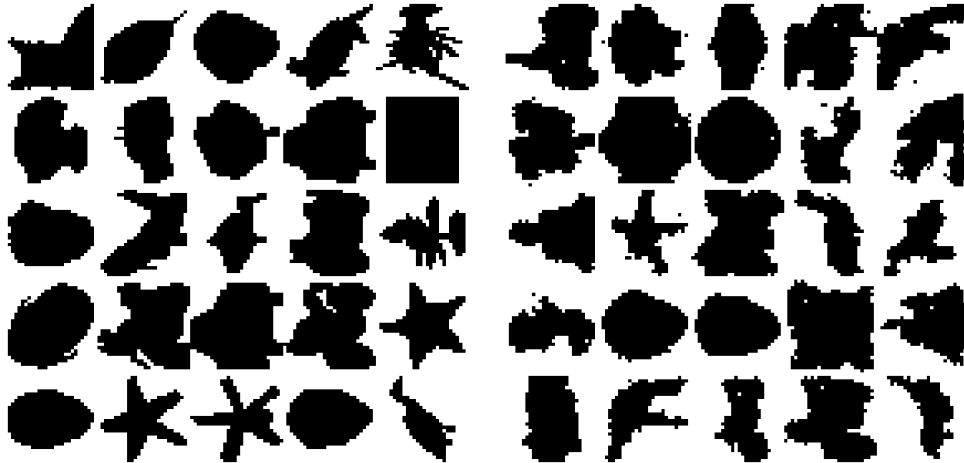


Figure 20: **Left:** A subset of FashionMNIST showing 25 random samples. **Right:** 25 images generated from the RBM trained of the FMNIST dataset. The RBM was trained up to $t_{age} \approx 200k$ and extracted at $t_G = k = 100$

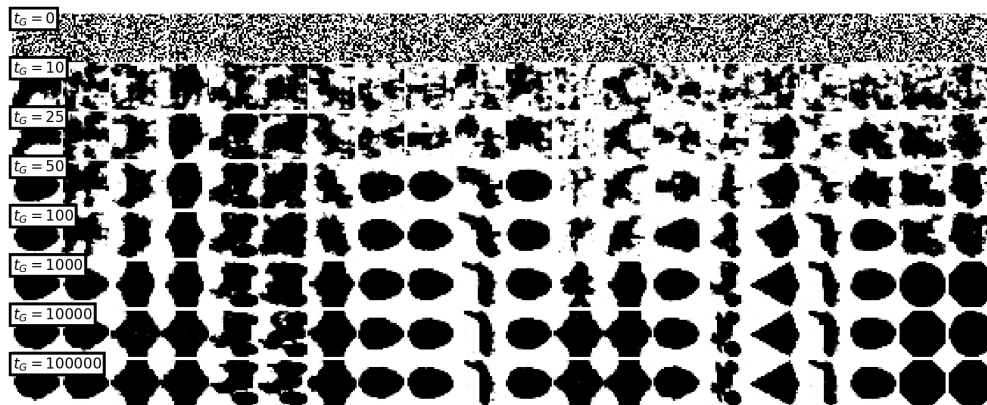


Figure 21: Various samples obtained from the RBM at different values of t_G . We see that when $t_G = k$ we obtain quite good samples while for large sampling time the generated images over-represent some shapes.

- Learning rate: $\alpha = 0.01$
- Minibatch size: $n_{mb} = 500$
- For the indicators, we used $N_s = 1000$ samples.
- During the training we used $k = 100$ Gibbs steps.
- the rest is the same as for MNIST.

We show on fig. 20 a subset of the dataset together with the generated images of the RBM. Then, we show on fig. 19 the results of several indicators for this case showing again the non-equilibrium regime when $t_G \approx k$. Finally, we show how the samples evolves on fig. 21 when we let the sampling for a large number of MC steps.

8 Results for smallNORB dataset

This dataset [10] corresponds to a total of 48600 images of 96×96 pixels in grayshade dividing in two sets of equals size (train and test). The images correspond to pictures of small toy taken under

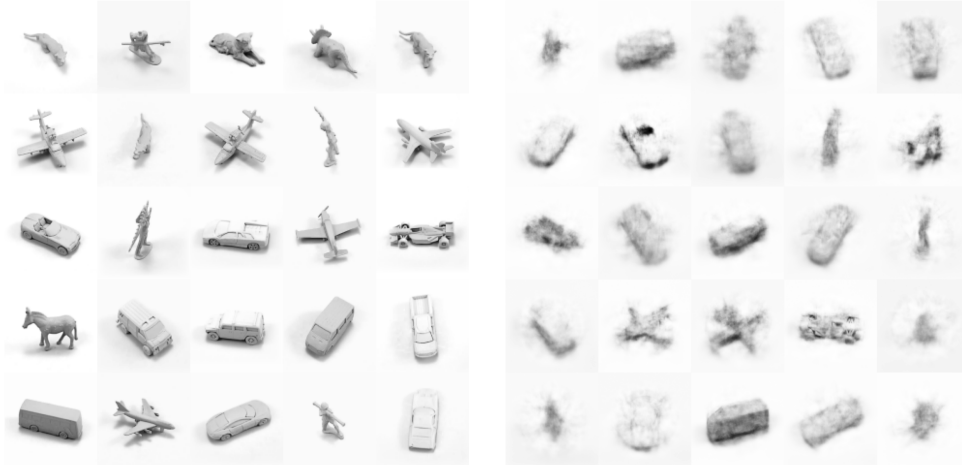


Figure 22: **Left:** A subset of FashionMNIST showing 25 random samples. **Right:** 25 images generated from the RBM trained of the FMNIST dataset. The RBM was trained up to $t_{\text{age}} \approx 200k$ and extracted at $t_G = k = 100$

different condition (light, angle ...). For the purpose of our work and to simplify the learning, we gather all the possible samples (amongst the train and test sets) selecting only one type of lighting. This reduced the dataset to 16300 images, which we refer to as NORB_REDUX. The RBM was trained on the gray shaded images using the following parameters:

- Number of hidden nodes: $N_h = 2000$
- Learning rate: $\alpha = 0.01$
- Minibatch size: $n_{mb} = 500$
- For the indicators, we used $N_s = 1000$ samples.
- During the training we used $k = 100$ Gibbs steps.
- the rest is the same as for MNIST.

We show on fig. 22 a subset of the dataset together with the generated images of the RBM. Then, we show on fig. 19 the results of several indicators for this case showing again the non-equilibrium regime when $t_G \approx k$. Finally, we show how the samples evolves on fig. 23 when we let the sampling for a large number of MC steps.

9 Results for CIFAR10 dataset

This dataset [11] corresponds to a total of 60k images of 10 classes of objects in color. The resolution of each image is 32×32 . Since the dataset is in color, the total number of input is 3×32^2 . The images correspond to pictures of celebrity. The RBM was trained on the colored images using the following parameters:

- Number of hidden nodes: $N_h = 1000$
- Learning rate: $\alpha = 0.01$
- Minibatch size: $n_{mb} = 500$
- For the indicators, we used $N_s = 1000$ samples.
- During the training we used $k = 100$ Gibbs steps.
- the rest is the same as for MNIST.

We show on fig. 24 a subset of the dataset together with the generated images of the RBM. Then, we show on fig. 19 the results of several indicators for this case showing again the non-equilibrium

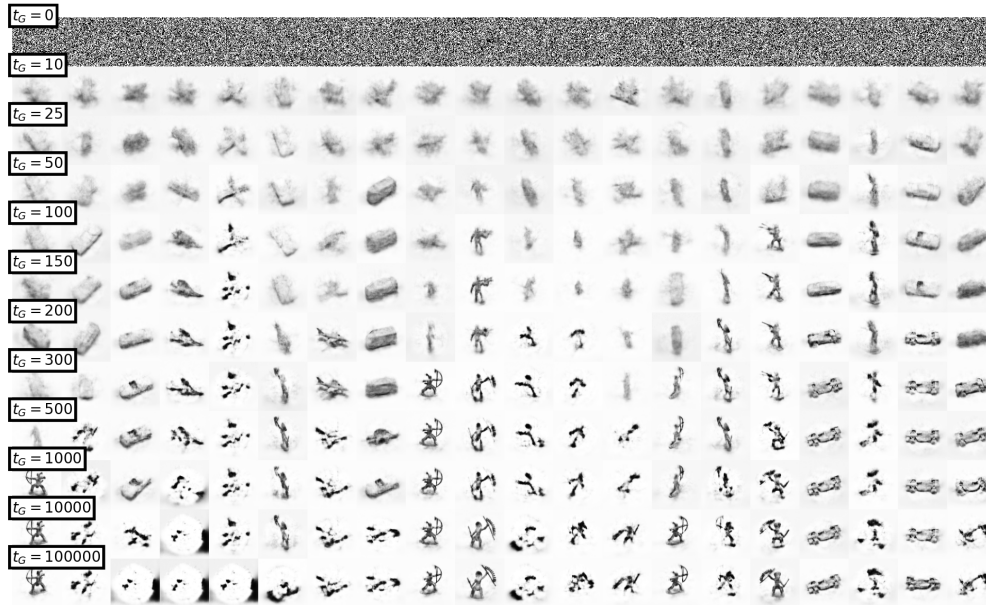


Figure 23: Various samples obtained from the RBM at different values of t_G . We see that when $t_G \approx k$ we obtain quite good samples while for large sampling time, the generated images are sometime based or only of a particular type.

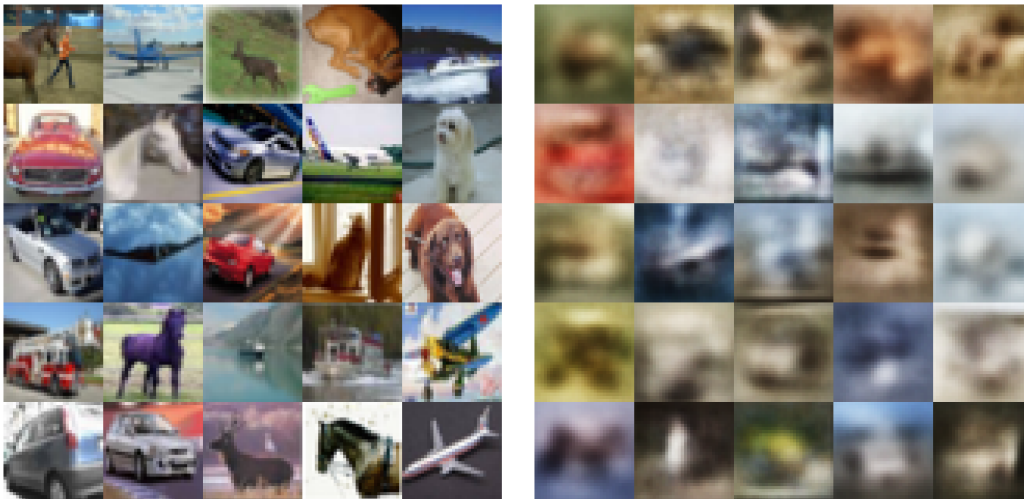


Figure 24: **Left:** A subset of CIFAR10 showing 25 random samples. **Right:** 25 images generated from the RBM trained of the CIFAR10 dataset. The RBM was trained up to $t_{\text{age}} \approx 900k$ and extracted at $t_G = k = 100$

regime when $t_G \approx k$. Finally, we show how the samples evolves on fig. 25 when we let the sampling for many MC steps.

10 Results for CelebA dataset

This dataset[12] corresponds to a total of more than 200k images of celebrity. For the purpose of our work, we retain only 12000 images, which we downsample to 64×64 pixels. Since the dataset

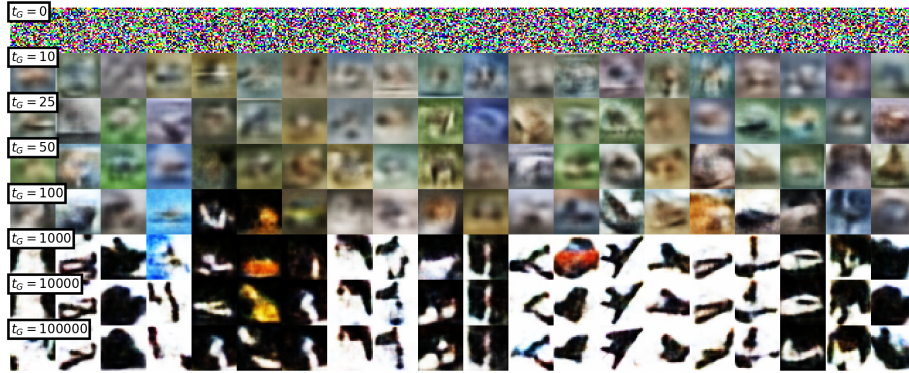


Figure 25: Various samples obtained from the RBM at different values of t_G . We see that when $t_G = k = 100$ we obtain samples with great variety while for large sampling time the generated images get a very biased look.

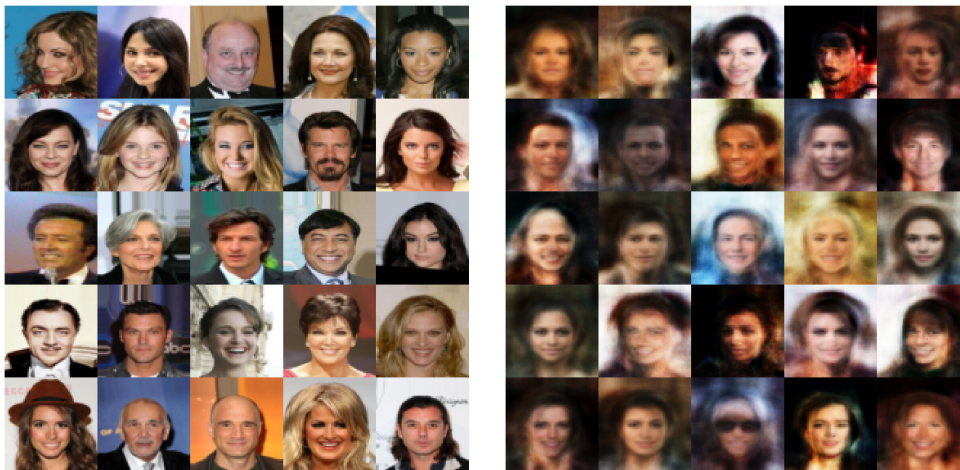


Figure 26: **Left:** A subset of CELEBA showing 25 random samples. **Right:** 25 images generated from the RBM trained of the CELEBA dataset. The RBM was trained up to $t_{\text{age}} \approx 100k$ and extracted at $t_G = k = 100$.

is in color, the total number of input is 3×64^2 . The images correspond to pictures of celebrity. The RBM was trained on the grayshaded images using the following parameters:

- Number of hidden nodes: $N_h = 5000$
- Learning rate: $\alpha = 0.01$
- Minibatch size: $n_{mb} = 500$
- For the indicators, we used $N_s = 1000$ samples.
- During the training we used $k = 100$ Gibbs steps.
- the rest is the same as for MNIST.

We show on fig. 26 a subset of the dataset together with the generated images of the RBM. Then, we show on fig. 19 the results of several indicators for this case showing again the non-equilibrium regime when $t_G \approx k$. Finally, we show how the samples evolves on fig. 27 when we let the sampling for many MC steps.



Figure 27: Various samples obtained from the RBM at different values of t_G . We see that when $t_G = k = 100$ we obtain quite good samples while for large sampling time the generated images over-represent more regular images.

References

- [1] Radford M Neal. Annealed importance sampling. *Statistics and computing*, 11(2):125–139, 2001.
- [2] Oswin Krause, Asja Fischer, and Christian Igel. Algorithms for estimating the partition function of restricted boltzmann machines. *Artificial Intelligence*, 278:103195, 2020.
- [3] Andrew Yale, Saloni Dash, Ritik Dutta, Isabelle Guyon, Adrien Pavao, and Kristin P Bennett. Generation and evaluation of privacy preserving synthetic health data. *Neurocomputing*, 416:244–255, 2020.
- [4] Martin Heusel, Hubert Ramsauer, Thomas Unterthiner, Bernhard Nessler, and Sepp Hochreiter. Gans trained by a two time-scale update rule converge to a local nash equilibrium. *Advances in neural information processing systems*, 30, 2017.
- [5] Jan Melchior, Asja Fischer, and Laurenz Wiskott. How to center deep boltzmann machines. *The Journal of Machine Learning Research*, 17(1):3387–3447, 2016.
- [6] Adam Paszke, Sam Gross, Francisco Massa, Adam Lerer, James Bradbury, Gregory Chanan, Trevor Killeen, Zeming Lin, Natalia Gimelshein, Luca Antiga, Alban Desmaison, Andreas Kopf, Edward Yang, Zachary DeVito, Martin Raison, Alykhan Tejani, Sasank Chilamkurthy, Benoit Steiner, Lu Fang, Junjie Bai, and Soumith Chintala. Pytorch: An imperative style, high-performance deep learning library. In *Advances in Neural Information Processing Systems 32*, pages 8024–8035. Curran Associates, Inc., 2019.
- [7] Vincenza Colonna, Qasim Ayub, Yuan Chen, Luca Pagani, Pierre Luisi, Marc Pybus, Erik Garrison, Yali Xue, and Chris Tyler-Smith. Human genomic regions with exceptionally high levels of population differentiation identified from 911 whole-genome sequences. *Genome biology*, 15(6):1–14, 2014.
- [8] Burak Yelmen, Aurélien Decelle, Linda Ongaro, Davide Marnetto, Corentin Tallec, Francesco Montinaro, Cyril Furtlehner, Luca Pagani, and Flora Jay. Creating artificial human genomes using generative neural networks. *PLoS genetics*, 17(2):e1009303, 2021.
- [9] Han Xiao, Kashif Rasul, and Roland Vollgraf. Fashion-mnist: a novel image dataset for benchmarking machine learning algorithms. *CoRR*, abs/1708.07747, 2017.
- [10] Yann LeCun, Fu Jie Huang, and Leon Bottou. Learning methods for generic object recognition with invariance to pose and lighting. In *Proceedings of the 2004 IEEE Computer Society Conference on Computer Vision and Pattern Recognition, 2004. CVPR 2004.*, volume 2, pages II–104. IEEE, 2004.
- [11] Alex Krizhevsky, Geoffrey Hinton, et al. *Learning multiple layers of features from tiny images*. Technical Report TR-2009, University of Toronto, Toronto., 2009.

- [12] Ziwei Liu, Ping Luo, Xiaogang Wang, and Xiaoou Tang. Deep learning face attributes in the wild. In *Proceedings of International Conference on Computer Vision (ICCV)*, December 2015.